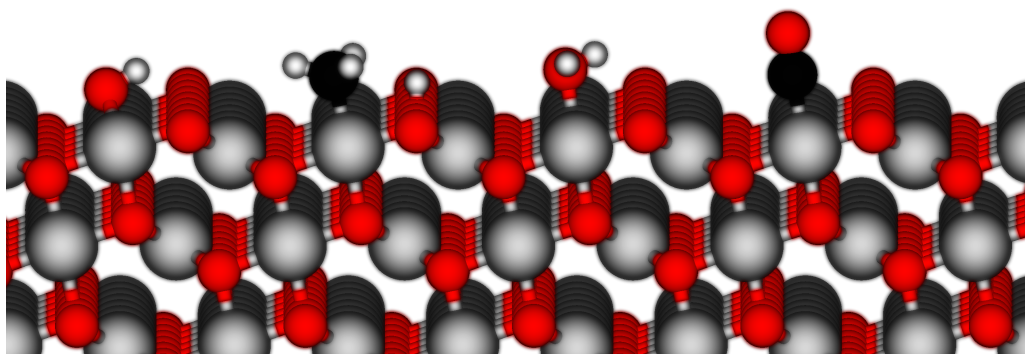




CHALMERS



Methane oxidation over palladium oxide: From electronic structure to catalytic conversion

MAXIME VAN DEN BOSSCHE

Department of Applied Physics
CHALMERS UNIVERSITY OF TECHNOLOGY
Gothenburg, Sweden 2015

Thesis for the degree of Licentiate of Engineering

**Methane oxidation over palladium oxide:
From electronic structure to catalytic conversion**

Maxime Van den Bossche



CHALMERS

Department of Applied Physics
Chalmers University of Technology
Gothenburg, Sweden 2015

Methane oxidation over palladium oxide:
From electronic structure to catalytic conversion
Maxime Van den Bossche

© Maxime Van den Bossche, 2015

Department of Applied Physics
Chalmers University of Technology
SE-412 96 Gothenburg
Sweden
Telephone: +46 (0)31-772 1000

Cover:

Ball-and-stick model of the PdO(101) surface with adsorbed species. The atomic colour codes are: gray – Pd, red – O, black – C, white – H.

Printed at Chalmers Reproservice
Gothenburg, Sweden 2015

Methane oxidation over palladium oxide:
From electronic structure to catalytic conversion

Maxime Van den Bossche
Department of Applied Physics
Chalmers University of Technology

Abstract

Understanding how catalysts work down to the atomic level can provide ways to improve chemical processes. The oxidation of methane is one such example, which is important from an environmental point of view. Methane is a potent greenhouse gas and natural and biogas vehicles need efficient catalysts to prevent slip of uncombusted fuel into the environment. Commercial catalysts for methane oxidation are often based on palladium or platinum. However, metallic palladium is easily converted to palladium oxide when the engine is operated at oxygen rich conditions.

In this thesis, various aspects of complete methane oxidation over PdO(101) are investigated with theoretical methods based on density functional theory (DFT). PdO(101) is recognised as the most active facet for the oxidation reaction. Firstly, adsorption configurations of the intermediates CO and H are studied in detail. By comparing calculated and measured core-level spectra, it is concluded that hydrogen adsorbs on undercoordinated palladium and oxygen atoms. CO is investigated also on the metallic Pd(111) surface and the adsorption mode is investigated as a function of surface oxidation using a combination of DFT calculations, core-level and infra-red spectroscopy.

Secondly, a first-principles microkinetic model is constructed that describes the catalytic conversion of CH₄ to CO₂ and H₂O over PdO(101). The kinetic modelling provides a more fundamental understanding of findings from reactor experiments, such as the rate limiting step and poisoning behaviour, and shows qualitatively different behaviour of reactions on oxide versus metal surfaces.

Lastly, limitations of the commonly used class of generalized gradient functionals are illustrated in the computation of core-level shifts and of thermodynamic and kinetic properties of adsorbates on the PdO(101) surface.

Keywords: heterogeneous catalysis, methane oxidation, palladium oxide, PdO(101), density functional theory, microkinetic modelling, core-level spectroscopy.

List of Publications

This thesis is based on the following appended papers:

Related publications not included in this thesis:

Trends in adsorbate induced core level shifts

V. Nilsson, M. Van den Bossche, A. Hellman, and H. Grönbeck
Surface Science (Accepted)

My contributions to the publications

Paper I

I performed all the calculations and co-authored the theoretical part of the paper.

Paper II

I performed all the calculations and co-authored the theoretical part of the paper.

Paper III

I performed all the calculations and co-authored the theoretical part of the paper.

Paper IV

I performed all the calculations, wrote the first draft and finalised the paper together with my co-authors.

Paper V

I performed all the calculations, wrote the first draft and finalised the paper together with my co-authors.

Contents

1 Introduction	1
1.1 Unravelling surface reactions	2
1.2 Objectives	3
2 Electronic structure	5
2.1 The electronic Hamiltonian	6
2.2 Density functional theory	7
2.2.1 The local density approximation	9
2.2.2 The generalized gradient approximation	11
2.2.3 Beyond the generalized gradient approximation	11
2.3 DFT in practice: the ‘PWPAW’ approach	13
2.3.1 Kohn-Sham DFT with a plane wave basis	14
2.3.2 The projector augmented-wave method	16
2.3.3 Finding the Kohn-Sham ground state	18
3 From electronic energies to measurable properties	21
3.1 Geometry optimisation	21
3.1.1 Finding a local minimum	21
3.1.2 Finding a transition state	22
3.2 Vibrational frequencies	23
3.3 Rates of reactions on surfaces	24
3.3.1 Transition state theory	24
3.3.2 Mean-field kinetic modelling	25
3.4 Core-level spectroscopy	26
3.4.1 The complete screening picture	27
3.4.2 Initial and final state contributions	28
4 Reactions on surfaces	29
4.1 Catalytic reactions	29
4.2 Bonding on surfaces	30
4.2.1 CO adsorbed on Pd(100)	31
4.2.2 CO adsorbed on PdO(101)	32
4.2.3 CO adsorbed on MgO(100)	33
5 Methane oxidation over PdO(101)	35
5.1 Introduction	35
5.2 Hydrogen adsorption	38
5.3 Carbon monoxide adsorption	38
5.4 Methane oxidation	39
5.5 Computational methodology	42
6 Conclusions and outlook	45
6.1 Outlook	46

Appendix	49
A Normal mode analysis	49
Acknowledgements	53
Bibliography	55

Chapter 1

Introduction

Our society currently faces challenges in all areas of sustainable development [1]. One of the most pressing environmental issues is the release of pollutants by human activity. Greenhouse gas (GHG) emissions are suspected to be the main cause for the observed global warming of the planet. A number of initiatives therefore aim to reduce these emissions. One example is the EU 2020 strategy [2], where one of the targets is to lower the GHG emissions by at least 20% by 2020 (compared to 1990).

Important anthropogenic GHGs include carbon dioxide, methane, chlorofluorocarbons and nitrous oxide [3]. While emissions of non-carbon dioxide GHGs, such as methane, are much lower than that of carbon dioxide, their contributions to the greenhouse effect are considerable due to their higher global warming potential (about ten times that of carbon dioxide on a molar basis for methane [4]). For methane, emission sources include agriculture, waste treatment, oil, gas and coal extraction and fuel combustion [5]. Where possible, it is preferable to oxidise the methane into carbon dioxide, which is a less harmful pollutant.

The contribution of methane emissions from the transportation and energy sector is expected to grow due to the increasing use of methane-based fuels, as an alternative to traditional fossil fuels [6]. The main reasons for this increase are (i) lower carbon dioxide emissions per unit of energy generated, (ii) lower particulate emissions compared to traditional fuels, (iii) the existence of large reserves of natural gas, and (iv) the possibility of using environmentally friendly biogas. Regarding the transportation sector, natural gas vehicles are especially common in several Asian and South American countries [7]. A more nearby example is the GoBiGas project [8] in Göteborg, where the aim is to produce biogas through gasification of biomass, so as to promote the use of biogas vehicles in the region. In the energy sector, natural and biogas power stations are on the rise, in part because efficient gas turbines are a common choice in high efficiency combined heat and power generation cycles [9].

Combustion engines running on methane-rich fuels are plagued by unburned methane slipping into the outlet. A similar issue is present in catalytic combustors used in gas turbines to burn the fuel at more moderate temperatures, so as to reduce e.g. NO_x

emissions [6]. To avoid increasing the temperature in order to burn away the remaining methane, a catalyst is generally used to speed up the oxidation.

Commercial catalysts are based on precious transition metals such as palladium or platinum [6]. These catalytically active materials are present as nanometer-sized particles dispersed on the surface of a porous support, such as alumina, silica or ceria. The methane and oxygen reactants present in the gas stream adsorb on the catalyst surface, where the subsequent chemical reactions between them take place. Aside from the ‘engineering’ problems in optimising the mass and heat flow through a catalytic reactor, there is still considerable room to improve the actual ‘chemistry’ happening on the catalyst. On the one hand, it is desirable to increase the intrinsic activity of these catalysts, so that more of the methane is being converted. On the other hand, decreasing (or even eliminating) the precious metal content allows a more efficient use of the limited precious metal reserves on Earth.

1.1 Unravelling surface reactions

In order to improve the catalytic activity and selectivity, it is beneficial to start with understanding of how the current catalysts are able to carry out the chemical process. Such insights in how technical catalysts work, however, can be hard to achieve. These materials can namely adopt various structures and compositions and are exposed to complex feed streams. One successful approach to this problem has been to reduce the catalyst to its essential part and thereby identifying and investigating the catalytically active material itself, without the support. A further disentanglement can be achieved by separately studying the different ideal crystal surfaces of the material under consideration. In order to perform detailed experiments, such as X-ray spectroscopy, also the pressure needs to be lowered to near vacuum.

Both the simplification of the material and the lowering of the pressures lead to a certain discrepancy between the studied material and the technical catalysts. This is called the ‘materials gap’ and ‘pressure gap’, respectively. However, once a firm understanding has been obtained on this level, the complexity can be gradually brought back in. Surface defects can for example be included, as well as effects of the support material and the behaviour at relevant pressures.

Computational physics and chemistry can have different roles to play in this process of understanding and improving catalytic materials. Electronic structure calculations can offer access to (in principle) all properties of a material starting from ‘first-principles’, i.e. from fundamental physical theories. This means that theoretical predictions can help the

interpretation of experimental measurements. Additionally, some properties can be more easily tackled from a theoretical point of view. Surface energies and detailed reaction kinetics are examples of such properties. Thirdly, a first-principles viewpoint has a high potential in the rational design of new, yet unsynthesised catalytic materials.

1.2 Objectives

The general aim of this thesis is to attain a more fundamental, molecular-level understanding of methane oxidation on transition metals and their oxides, especially palladium oxide, using theoretical methods. Additionally, the total oxidation of methane can serve as a model system for the oxidation of more complex hydrocarbons and can also yield insights regarding partial oxidation reactions, e.g. from methane to methanol. The different elements of this licentiate thesis are represented in Figure 1.1.

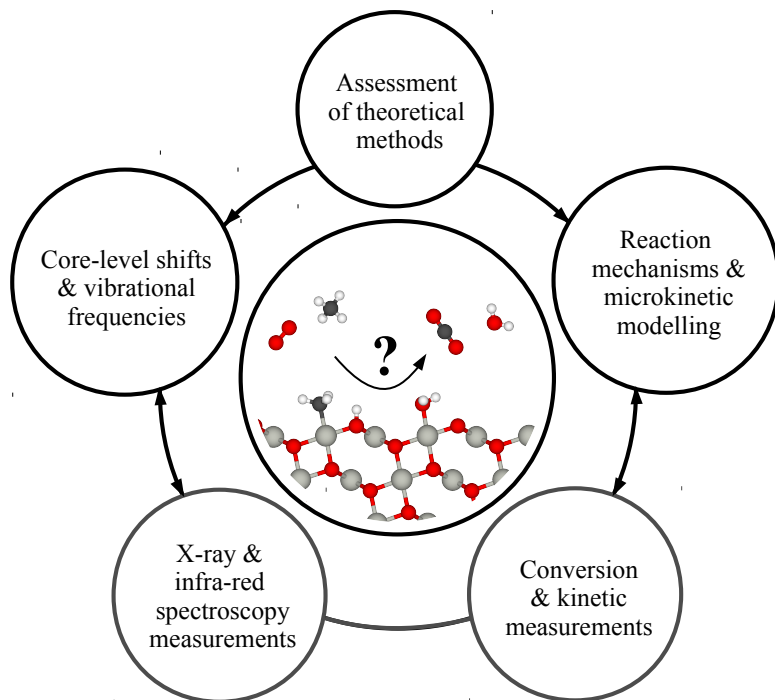


Figure 1.1: Schematic representation of the different elements used in this thesis to unravel methane oxidation over palladium oxide.

Several aspects of methane oxidation have been investigated during the course of this work. The approach has been to build up the complexity in steps, with continued feedback between computations and experiments. On one hand, density functional theory studies were performed addressing the subprocesses of the methane oxidation reaction. These are the interaction of carbon monoxide and hydrogen with the oxidized palladium surfaces, in connection to experimental spectroscopic measurements. Secondly, a detailed kinetic model was built for the complete conversion of methane over the PdO(101) surface, providing a more fundamental understanding of experimental reactor data. Lastly, also the accuracy of the employed computational methods has been investigated.

Chapter 2

Electronic structure

“*The underlying physical laws necessary for the mathematical theory of a large part of physics and the whole of chemistry are thus completely known, and the difficulty is only that the exact application of these laws leads to equations much too complicated to be soluble. It therefore becomes desirable that approximate practical methods of applying quantum mechanics should be developed, which can lead to an explanation of the main features of complex atomic systems without too much computation.*

– Paul Dirac [10]

The above statement by Dirac in 1929 points to the problem when applying quantum mechanics to chemical problems. Solids and molecules are made up of electrons and nuclei, which can, in principle, be exactly described by a many-body wave function obtained by solving the Schrödinger (or Dirac) wave equation. Unlike the classical N -body problem, the quantum many-body problem can only be solved exactly in the case of one-electron systems. This is due to the fact that the many-body wave function must not only reflect the Coulomb interactions between the particles, but must also obey certain symmetries with respect to the exchange of two particles.

As a consequence, different approaches have been advanced to find an approximate solution to the Schrödinger equation for many-particle systems. The two most widely used families of methods are those based on Hartree-Fock theory and Density Functional Theory (DFT). For problems involving surfaces and where structural models with tens of atoms are considered, DFT is frequently the method of choice.

The following sections give an introduction to DFT and an example of how it can be implemented in a practical computer code. First, however, two additional approximations will be made. While DFT in general is not bound by these approximations, they are routinely applied and are standard in the study of chemical problems.

2.1 The electronic Hamiltonian

A general approximation is the Born-Oppenheimer approximation, where the electrons are assumed to stay in the same adiabatic eigenstate when the coordinates of the nuclei are changed. This means that the electronic and nucleic motions are considered to be decoupled and that the many-body wave function can be written as the product of an electronic and a nucleic wave function. The electronic wave function obeys an electronic Schrödinger equation, with an external potential that depends on the instantaneous positions of the nuclei. The potential energy in the nucleic Schrödinger equation, in turn, depends on the electronic eigenstate (e.g. the ground state). This assumption is typically valid except if the nuclei are moving fast and the electronic energy levels are closely spaced. In other words, the nuclei are stationary from the electrons' point of view and one can focus on only solving the electronic Schrödinger equation, for given positions of the nuclei.

Another approximation is that the electrons are treated as non-relativistic particles, which is justified as long as they do not reach relativistic speeds. This is commonly the case for the valence electrons. Core electrons, however, require a relativistic treatment for elements starting from the fourth row [11]. These effects are handled in a separate way (as discussed in Section 2.3.2). This is important because a relativistic treatment of the core electrons will affect the electronic spectrum also in the valence.

Under the approximations described above, the time-independent electronic wave function $\Psi(\mathbf{r}_1, \dots, \mathbf{r}_N)$ for a set of N electrons (of a closed shell system) in the presence of M nuclei obeys the Schrödinger equation:

$$E_l \Psi_l(\mathbf{r}_1, \dots, \mathbf{r}_N) = H \Psi_l(\mathbf{r}_1, \dots, \mathbf{r}_N) \quad (2.1)$$

The Hamiltonian H is the sum of kinetic and potential energy operators (in atomic units):

$$H = T + V_{\text{ext}} + V_{\text{el}} \quad (2.2)$$

$$T = -\frac{1}{2} \sum_i^N \left(\frac{\partial^2}{\partial x_i^2} + \frac{\partial^2}{\partial y_i^2} + \frac{\partial^2}{\partial z_i^2} \right) \quad (2.3)$$

$$= -\frac{1}{2} \sum_i^N \nabla_i^2 \quad (2.4)$$

$$V_{\text{ext}} = \sum_i^N \sum_j^M \frac{Z_j}{|\mathbf{R}_j - \mathbf{r}_i|} \quad (2.5)$$

$$V_{\text{el}} = \sum_i^N \sum_j^i \frac{1}{|\mathbf{r}_j - \mathbf{r}_i|} \quad (2.6)$$

Here, the external potential V_{ext} represents the Coulomb attraction of the electrons to the nuclei and V_{el} the potential arising from the Coulomb repulsion between the electrons.

2.2 Density functional theory

Already in 1927 alternative approaches to the Schrödinger equation were formulated by Thomas and Fermi [13, 14] that relied on the electron *density* as a central variable, rather than the intractable many-body wave function. However, these methods lacked a rigorous basis until Hohenberg and Kohn [15] showed in 1964 that there exists a functional F that maps the electron density function $\rho(\mathbf{r})$ to the electronic energy E :

$$E = F[\rho(\mathbf{r})] = F[\rho] \quad (2.7)$$

If contributions from the external potential and from the classical Coulomb (‘Hartree’) potential are separated from F , one obtains:

$$E = E_{\text{ext}}[\rho] + E_{\text{Hartree}}[\rho] + G[\rho] \quad (2.8)$$

$$E_{\text{ext}}[\rho] = \frac{1}{2} \int V_{\text{ext}}(\mathbf{r})\rho(\mathbf{r})d\mathbf{r} \quad (2.9)$$

$$V_{\text{ext}}(\mathbf{r}) = \sum_j^M \frac{Z_j}{|\mathbf{R}_j - \mathbf{r}|} \quad (2.10)$$

$$E_{\text{Hartree}}[\rho] = \frac{1}{2} \int V_{\text{Hartree}}(\mathbf{r})\rho(\mathbf{r})d\mathbf{r} \quad (2.11)$$

$$V_{\text{Hartree}}(\mathbf{r}) = \int \frac{\rho(\mathbf{r}')}{|\mathbf{r} - \mathbf{r}'|} d\mathbf{r}' \quad (2.12)$$

The Hohenberg-Kohn theorem implies that we can use the density $\rho(\mathbf{r})$ instead of the many-body wave function $\Psi(\mathbf{r}_1, \dots, \mathbf{r}_N)$ to obtain various electronic properties. While this approach is potentially much more efficient, the exact form of the functional G is unknown to this date, and will probably remain so for an indefinite time to come.

One particularly successful approach to use this result by Hohenberg and Kohn is that by Kohn and Sham [16], which is largely responsible for the wide popularity of DFT schemes. They showed that the ground state density and energy can be obtained by solving a set of one-electron equations instead of solving the many-electron problem. This

can be achieved by separating out the kinetic energy of non-interacting electrons from $G[\rho]$ (with ψ_i the one-electron orbitals):

$$G[\rho] = T_{\text{non-int}}[\rho] + E_{\text{xc}}[\rho] \quad (2.13)$$

$$T_{\text{non-int}}[\rho] = -\frac{1}{2} \sum_i^N \langle \psi_i | \nabla^2 | \psi_i \rangle \quad (2.14)$$

The electron density, given by the square of the one-electron orbitals,

$$\rho(\mathbf{r}) = \sum_i^N \langle \psi_i | \psi_i \rangle \quad (2.15)$$

is equal to the true electron density if the independent electrons obey the single-particle Kohn-Sham equations. These equations are given by:

$$\left(-\frac{1}{2} \nabla^2 + v_{\text{eff}}(\mathbf{r}) \right) \psi_i(\mathbf{r}) = \epsilon_i \psi_i(\mathbf{r}) \quad (2.16)$$

with the effective single-particle potential v_{eff} determined as:

$$v_{\text{eff}}(\mathbf{r}) = v_{\text{ext}}(\mathbf{r}) + v_{\text{Hartree}}(\mathbf{r}) + v_{\text{xc}}(\mathbf{r}) \quad (2.17)$$

$$v_{\text{xc}}(\mathbf{r}) = \frac{\partial E_{\text{xc}}[\rho]}{\partial \rho(\mathbf{r})} \quad (2.18)$$

The set of Kohn-Sham equations is to be solved self-consistently (see subsection 2.3.3), under the constraint that the integrated density equals the number of electrons N . The total energy in the Kohn-Sham approach equals:

$$E_{\text{tot}} = T_{\text{non-int}} + E_{\text{ext}} + E_{\text{Hartree}} + E_{\text{xc}} \quad (2.19)$$

It may seem peculiar to reintroduce the orbitals in a formalism based on the density, as it noticeably increases the complexity compared to using the total electron density alone. However, with this approach, the kinetic energy is well described, which is critical in e.g. describing chemical bonds [17].

Due to their non-interacting nature, the one-electron orbitals and eigenvalues generally do not have a rigorous meaning. The eigenvalues do not exactly correspond to an ionisation potential, unlike the eigenvalues in Hartree-Fock theory (Koopman's theorem [18]). The exception is the eigenvalue of the highest occupied state in a finite system, which (with the exact functional) corresponds to the negative of the first electronically relaxed ionisation

potential [19]. Another consequence of the non-interacting nature of the Kohn-Sham system is that the total energy of the interacting system is not simply equal to the sum of the Kohn-Sham eigenvalues, but rather:

$$E_{\text{tot}} = \sum_i^N \epsilon_i - E_{\text{Hartree}}[\rho] + E_{\text{xc}}[\rho] - \int \rho(\mathbf{r})v_{\text{xc}}(\mathbf{r})d\mathbf{r} \quad (2.20)$$

It is clear that the potential benefits of the Kohn-Sham approach are huge, as such an independent-particle problem is tremendously easier to solve than the original many-body problem. The difficulties now lie in the exchange-correlation functional E_{xc} , which is the term where all the difficult quantities are hidden and where approximations are needed. Effects that E_{xc} should capture are:

- (i) Owing to the fermionic nature of the electron, the many-body wavefunction must change sign when two electrons are exchanged (cfr. the Pauli exclusion principle). This is generally referred to as ‘electronic exchange’. This anti-symmetry requirement ultimately results in a larger spatial separation between electrons, which results in a lowering of the electronic repulsion. Moreover, the nuclear charge is in this way less effectively screened.
- (ii) Other effects are also present from the purely classical interactions between the electrons. The effect of ‘instantaneous’ Coulomb correlation, for example, is not captured by the mean-field character of the Hartree energy expression. Additionally, the self-interaction error in the Hartree term needs to be corrected. The Hartree energy namely contains artificial interactions of the electrons with themselves, which is clearly visible in the case of one electron where the Hartree energy is non-zero. Lastly, E_{xc} should also take into account the difference in kinetic energy of the interacting and non-interacting electrons.

2.2.1 The local density approximation

The strength of the Kohn-Sham DFT approach lies in the fact that there exist clever yet rather simple approximations to the exchange-correlation functional which can yield quite accurate results. In the local density approximation (LDA), the density is assumed to be sufficiently slowly varying, so that:

$$E_{\text{xc}}[\rho] = \int \rho(\mathbf{r})\epsilon_{\text{xc}}^{\text{hom}}(\rho)d\mathbf{r} \quad (2.21)$$

with $\epsilon_{xc}^{hom}[\rho]$ the exchange-correlation energy per electron in a homogeneous electron gas with density ρ . For the exchange part, the exact analytical solution is known [12] and analytical expressions for the correlation energy density are obtained by parametrisation of exact quantum Monte Carlo simulations of the homogeneous electron gas. Eq. (2.24)-(2.25) show the parametrization by Perdew and Zunger [20] of the simulation results of Ceperley and Alder [21].

$$\epsilon_{xc}^{LDA}(\rho) = \epsilon_x^{hom}(\rho) + \epsilon_c^{hom}(\rho) \quad (2.22)$$

$$\epsilon_x^{hom}(r_s) = -\frac{3}{4\pi} \sqrt[3]{\frac{9\pi}{4}} \frac{1}{r_s} \quad (2.23)$$

$$\epsilon_c^{hom}(r_s) = -0.048 + 0.0311 \ln r_s + 0.0020 r_s \ln r_s - 0.0116 r_s \quad , \quad r_s < 1 \quad (2.24)$$

$$= \frac{-0.1423}{1 + 1.0529\sqrt{r_s} + 0.3334r_s} \quad , \quad r_s \geq 1 \quad (2.25)$$

The variable r_s corresponds to the radius of a sphere containing one electron on average:

$$r_s(\mathbf{r}) = \sqrt[3]{\frac{3}{4\pi\rho(\mathbf{r})}} \quad (2.26)$$

Given its simplicity, the LDA works well for extended systems with slowly varying electron densities in the bonding region, as in bulk solids (in particular free-electron metals such as aluminium). Equilibrium unit cell volumes and bulk moduli are typically obtained with mean average relative errors of circa 5% and 20% with respect to experiment [22]. In such cases, the exchange and correlation effects are naturally well described within the LDA. Moreover, when the orbitals are delocalised over the whole structure, the self-interaction error in the Hartree term is small [20].

When the orbitals become more localised, as in atoms and molecules, this self-interaction error increases. This is cancelled, though only partially, by errors in the exchange-correlation energy [20]. This leads, for example, to the tendency for the LDA to ‘overbind’ [23], i.e. to overestimate binding energies and slightly underestimate bond distances. This is for example visible in Pople’s G2-1 data set, which consists of consists of 55 small molecules with well-established experimental atomization energies, ionization potentials, electron affinities and proton affinities [24, 25] and is frequently used in the assessment of electronic structure methods. In this data set, the mean absolute error in the atomization energies with respect to experiment amounts to a considerable 1.6 eV [26].

2.2.2 The generalized gradient approximation

Overall (and especially for atoms and molecules) a significant improvement is obtained when including the effect of the magnitude of the gradient of the density on the exchange-correlation energy. One family of such functionals are the generalized gradient approximation (GGA) functionals, to which the Perdew-Wang (PW91) [27] and Perdew-Burke-Ernzerhof (PBE) [28] functionals belong:

$$E_{xc}^{GGA}[\rho] = E_x^{GGA}[\rho] + E_c^{GGA}[\rho] \quad (2.27)$$

$$E_x^{GGA}[\rho] = \int \rho(\mathbf{r}) \epsilon_x^{hom}(\rho) F_x(\rho, |\nabla\rho|) d\mathbf{r} \quad (2.28)$$

$$E_c^{GGA}[\rho] = \int \rho(\mathbf{r}) \epsilon_c^{hom}(\rho) F_c(\rho, |\nabla\rho|) d\mathbf{r} \quad (2.29)$$

Regarding binding energies, GGA functionals now have a tendency to ‘underbind’, but deliver a much improved accuracy for a limited increase in computational cost. The mean absolute error in the atomization energies of the G2-1 data is 0.37 eV with the PBE functional [26], which is a decrease by a factor of four compared to the LDA. Quantitative (and in a few cases qualitative) accuracy is, however, still hindered by the incomplete cancellation of the self-interaction error, as well as an inadequate description of strong correlation effects. This leads, for example, to a consistent underestimation of band gaps [20], with even some strongly correlated semiconductors and insulators being described as metals (e.g. CoO).¹

2.2.3 Beyond the generalized gradient approximation

Several methods exist that remedy shortcomings of LDA and GGA functionals. For improved description of the correlation energy, methods based on the random phase approximation (RPA) can be used [30, 31], albeit at much increased computational cost. Specifically including long-range correlation of the van der Waals type into the functional is possible in the so-called van der Waals density functional (vdW-DF [32]).

Several other methods aim to reduce the self-interaction error in the LDA and GGA functionals. ‘Self-interaction correction’ (SIC) methods, for example, aim to avoid the self-interaction error by making each orbital experience a Hartree potential excluding its own charge density [20, 33]. The ‘+U’ approaches also introduce an orbital dependent

¹This seems, however, to also be related to the fact that even the exact Kohn-Sham band gap does not necessarily correspond to the gap measured experimentally [29].

potential, but do this by adding a repulsive Coulomb term between strongly correlated electrons on the same atom (typically $3d$ or $4f$), in the spirit of the Hubbard model [34]. This reduces the self-interaction error of partially occupied orbitals [35, 36]. This thesis features the use of so-called hybrid functionals, where a fraction α of the GGA exchange energy is replaced by the Hartree-Fock exchange energy of the occupied Kohn-Sham orbitals:

$$E_{xc}^{hybr} = \alpha E_x^{HF} + (1 - \alpha) E_x^{GGA} + E_c^{GGA} \quad (2.30)$$

$$E_x^{HF} = -\frac{1}{2} \sum_{i,j}^{occ.} \langle \psi_i \psi_j | v_x^{HF} | \psi_j \psi_i \rangle \quad (2.31)$$

$$= -\frac{1}{2} \sum_{i,j}^{occ.} \int \int \frac{\psi_i^*(\mathbf{r}) \psi_j(\mathbf{r}) \psi_j^*(\mathbf{r}') \psi_i(\mathbf{r}')}{|\mathbf{r} - \mathbf{r}'|} d\mathbf{r} d\mathbf{r}' \quad (2.32)$$

In the PBE0 hybrid functional, one quarter of Hartree-Fock exchange ($\alpha = 1/4$) is used in the PBE GGA functional [37], as motivated by the adiabatic connection theorem. A hybrid functional such as PBE0 substantially improves the description of geometries, thermochemistry and band gaps over the GGA functional PBE for both molecules and solids [38, 26, 39, 40], though the GGA functional remains more accurate for certain metallic systems [39, 40]. The mean absolute error in the atomization energies of the G2-1 data set is further reduced to 0.15 eV with PBE0 [26], compared to 0.37 with PBE. This improvement can be attributed, at least partially, to the reduction of the self-interaction error in the Hartree term by a similar ‘self-exchange’ error in the exchange term [41].

An important drawback of ‘global’ hybrid functionals, such as PBE0, is that the non-locality of the exchange functional in Eq. (2.31) severely worsens the scaling of the computational cost with the number of electrons. For more efficient calculations on extended systems such as bulk materials or surfaces, it can be beneficial to neglect the minor contribution of the long-range part of the exact exchange interaction by screening the exchange potential. This results in the so-called ‘range-separated’ hybrid functionals, such as the Heyd-Scuseria-Ernzerhof (HSE) functionals [42, 43, 44]. In the HSE functionals, the exchange potential is screened using the complement of the error function:

$$E_{xc}^{HSE} = \alpha E_x^{HF,SR}(\omega) + (1 - \alpha) E_x^{PBE,SR}(\omega) + E_x^{PBE,LR}(\omega) + E_c^{PBE} \quad (2.33)$$

$$v_x^{HF,SR}(\mathbf{r}, \mathbf{r}') = \frac{1 - \text{erf}(\omega|\mathbf{r} - \mathbf{r}'|)}{|\mathbf{r} - \mathbf{r}'|} \quad (2.34)$$

The short- and long-range exchange potential is shown in Figure 2.1. The screening

parameter ω has to be set small enough to retain agreement with the parent PBE0 functional, but as large as possible to improve the computational efficiency. Additionally, the accuracy in the G2-1 data set can actually be slightly enhanced over the PBE0 functional in a certain range of ω values. Based on these considerations, the optimal value for ω is chosen to be 0.11 Bohr^{-1} in the HSE06 functional (with $\alpha = 0.25$). There is, hence, a slight semi-empirical touch to the HSE functionals.

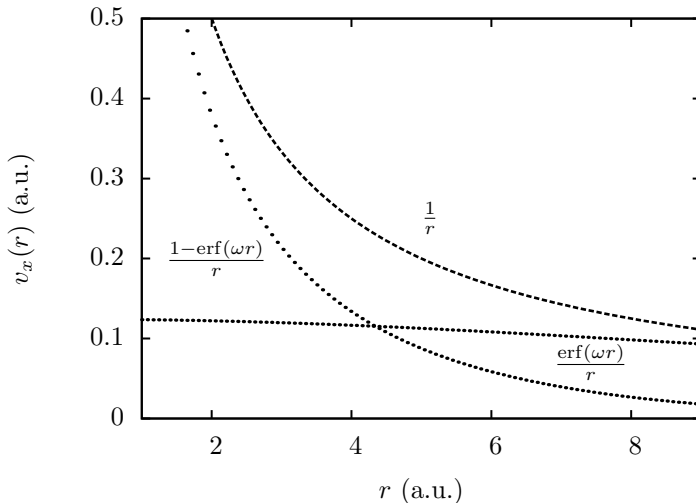


Figure 2.1: Plot of the Coulomb potential and its decomposition into long- and short-range parts using the error function for $\omega = 0.11 \text{ Bohr}^{-1}$.

2.3 DFT in practice: the ‘PWPAAW’ approach

Like in the case of the functionals, there is a wide variety of approaches addressing the more ‘technical’ aspects of electronic structure calculations. One of these aspects is the basis set in which the wave functions are expanded. One straightforward option is to use a uniform real-space grid, as in the GPAW code [45, 46]. Another is to use a basis set of local functions centred around each atom, e.g. Gaussian-type functions. When applying periodic boundary conditions, plane waves are a natural choice owing to their inherent periodicity.

Another aspect is how to treat the different behaviour of core and valence electrons. Popular choices here are methods based on pseudopotentials and all-electron methods

such as the projector augmented-wave (PAW) method. As the VASP code is a plane wave PAW code, it is these techniques that are given attention in the following paragraphs.

2.3.1 Kohn-Sham DFT with a plane wave basis

Felix Bloch proved [47] that a one-electron Schrödinger equation with a periodic Hamiltonian has solutions which can be written as:

$$\psi_{\mathbf{k}}(\mathbf{r}) = u_{\mathbf{k}}(\mathbf{r}) \exp(i\mathbf{k} \cdot \mathbf{r}) \quad (2.35)$$

The \mathbf{k} -vectors reside in the reciprocal space² spanned by the basis vectors \mathbf{b}_i :

$$\mathbf{k} = \sum_{i=1}^3 k_i \mathbf{b}_i, \quad k_i \in \mathbb{R} \quad (2.36)$$

$$\mathbf{b}_1 = 2\pi \frac{\mathbf{a}_2 \times \mathbf{a}_3}{\mathbf{a}_1 \cdot (\mathbf{a}_2 \times \mathbf{a}_3)} \quad (2.37)$$

where \mathbf{a}_i are the real space lattice vectors (\mathbf{b}_2 and \mathbf{b}_3 follow by permutation). The function $u_{\mathbf{k}}(\mathbf{r})$ has the periodicity of the crystal, as has the potential energy operator (here in the form of the effective Kohn-Sham potential $v_{\text{eff}}(\mathbf{r})$), which means they can be represented using Fourier series. The relationships between $u_{\mathbf{k}}(\mathbf{r})$ and its Fourier coefficients $\hat{u}_{\mathbf{k}}(\mathbf{G})$ are:

$$u_{\mathbf{k}}(\mathbf{r}) = \sum_{\mathbf{G}} \hat{u}_{\mathbf{k}}(\mathbf{G}) \exp(i\mathbf{G} \cdot \mathbf{r}) \quad (2.38)$$

$$\hat{u}_{\mathbf{k}}(\mathbf{G}) = \frac{1}{V_{\text{cell}}} \int_{V_{\text{cell}}} u_{\mathbf{k}}(\mathbf{r}) \exp(-i\mathbf{G} \cdot \mathbf{r}) d\mathbf{r} \quad (2.39)$$

with \mathbf{G} vectors of the reciprocal lattice ($\mathbf{G} = \sum_{i=1}^3 G_i \mathbf{b}_i$, $G_i \in \mathbb{Z}$).

The wave functions in general do not have the periodicity of the lattice, but are shifted in phase by a factor $\exp(i\mathbf{k} \cdot \mathbf{R})$ upon translation by a real space lattice vector $\mathbf{R} = \sum_{i=1}^3 N_i \mathbf{a}_i$, $N_i \in \mathbb{Z}$. For these we can write:

$$\psi_{\mathbf{k}}(\mathbf{r}) = \left(\sum_{\mathbf{G}} \hat{u}_{\mathbf{k}}(\mathbf{G}) \exp(i\mathbf{G} \cdot \mathbf{r}) \right) \exp(i\mathbf{k} \cdot \mathbf{r}) \quad (2.40)$$

$$= \sum_{\mathbf{G}} \hat{u}_{\mathbf{k}}(\mathbf{G}) \exp(i(\mathbf{k} + \mathbf{G}) \cdot \mathbf{r}) \quad (2.41)$$

²Reciprocal space can be thought of as the three-dimensional and spatial analogue of the Fourier (frequency) space of a time-periodic function.

If these expressions for $\psi_{\mathbf{k}}$ and v_{eff} are substituted in the real space Kohn-Sham equation,

$$\left(-\frac{1}{2}\nabla^2 + v_{\text{eff}}(\mathbf{r})\right)\psi_{\mathbf{k}}(\mathbf{r}) = \epsilon_{\mathbf{k}}\psi_{\mathbf{k}}(\mathbf{r}) \quad (2.42)$$

the corresponding expression in reciprocal space becomes:

$$\frac{1}{2}|\mathbf{k} + \mathbf{G}|^2\hat{u}_{\mathbf{k}}(\mathbf{G}) + \sum_{\mathbf{G}'}\hat{v}_{\text{eff}}(\mathbf{G} - \mathbf{G}')\hat{u}_{\mathbf{k}}(\mathbf{G}') = \epsilon_{\mathbf{k}}\hat{u}_{\mathbf{k}}(\mathbf{G}) \quad (2.43)$$

The eigenvalues and the Fourier coefficients $\hat{u}_{\mathbf{k}}(\mathbf{G})$ of the wave function are obtained by finding the eigenvalues and eigenvectors of the Hamiltonian matrix with elements:

$$H_{\mathbf{G},\mathbf{G}'}(\mathbf{k}) = \frac{1}{2}|\mathbf{k} + \mathbf{G}|^2\delta_{\mathbf{G},\mathbf{G}'} + \hat{v}_{\text{eff}}(\mathbf{G} - \mathbf{G}') \quad (2.44)$$

In practice, there is a need to truncate the number of reciprocal lattice vectors, which is done by considering only those vectors corresponding to a kinetic energy smaller than a certain energy cut-off value ($\frac{1}{2}|\mathbf{k} + \mathbf{G}|^2 < E_{\text{cut}}$). This is appropriate as the magnitude of the terms in a Fourier series decreases rapidly as the norm of the frequency vector increases.

The problem now boils down to solving this eigenvalue problem for all $\mathbf{k} \in \mathbb{R}^3$. However, it follows from Bloch's theorem (Eq. (2.35)) that if $\psi_{\mathbf{k}}$ is a solution, then so is $\psi_{\mathbf{k}+\mathbf{G}}$. The solutions can therefore be restricted to \mathbf{k} -vectors inside a primitive unit cell of the reciprocal space (such as the first Brillouin zone). Now there are different solutions $\psi_{\mathbf{k},n}$ for such a \mathbf{k} , which are labeled by the band index $n = 0, 1, 2, \dots$, with progressively higher eigenenergies $\epsilon_{\mathbf{k},n}$. In practice, the \mathbf{k} -dependence is handled through a discrete sampling of the (first) Brillouin zone. Additionally, only a finite number of bands needs to be considered, since there are only a finite number of electrons per unit cell.

The \mathbf{k} -point sampling in the calculations in this thesis is performed with the widely used method of Monkhorst and Pack [48, 49]. It consists of selecting \mathbf{k} -points according to a uniform ($N_1 \times N_2 \times N_3$) grid (N_i \mathbf{k} -points along the i^{th} reciprocal axis):

$$\mathbf{k}_{n_1,n_2,n_3} = \sum_{i=1}^3 \frac{2n_i - N_i - 1}{2N_i} \mathbf{b}_i, \quad n_i \in \{1 \dots N_i\} \quad (2.45)$$

The mesh needs to be sufficiently dense such that the Brillouin zone is sufficiently sampled to yield converged total energies. The set of \mathbf{k} -points for which the Hamiltonian needs to be diagonalized is further reduced by only considering the *irreducible* Brillouin zone, from which the contributions of the other \mathbf{k} -points can be deduced by symmetry

operations (with appropriate weighting).

The different contributions to the Kohn-Sham potential $\hat{v}_{\text{eff}}(\mathbf{G})$ and the total electronic energy are obtained from the Hartree potential, the external potential arising from the nuclei, and the exchange-correlation potential. An expression for the Hartree energy (see Eq.(2.11)) can be derived starting from the Poisson equation in real space:

$$\nabla^2 v_{\text{Hartree}}(\mathbf{r}) = -4\pi\rho(\mathbf{r}) \quad (2.46)$$

After substitution of the Fourier expansions, this yields the corresponding expression in reciprocal space:

$$\hat{v}_{\text{Hartree}}(\mathbf{G}) = \frac{4\pi\hat{\rho}(\mathbf{G})}{|\mathbf{G}|^2} \quad (2.47)$$

Using Plancherel's theorem [50], the Hartree energy per unit cell is given by:

$$E_{\text{Hartree}} = \frac{1}{2} \int_{V_{\text{cell}}} v_{\text{Hartree}}(\mathbf{r})\rho(\mathbf{r})d\mathbf{r} = 2\pi V_{\text{cell}} \sum_{\mathbf{G} \neq \mathbf{0}} \frac{\hat{\rho}(\mathbf{G})^2}{|\mathbf{G}|^2} \quad (2.48)$$

The divergent term for $\mathbf{G} = \mathbf{0}$ has been omitted, as it cancels with the corresponding term in the electron-nucleus attraction energy provided the unit cell has no net charge. The results for the external potential can be obtained in a similar way:

$$\nabla^2 v_{\text{ext}}(\mathbf{r}) = 4\pi \sum_m Z_m \delta(|\mathbf{r} - \mathbf{R}_m|) \quad (2.49)$$

$$\hat{v}_{\text{ext}}(\mathbf{G}) = -4\pi \sum_m Z_m \exp(-i\mathbf{G} \cdot \mathbf{R}_m) \frac{1}{|\mathbf{G}|^2} \quad (2.50)$$

$$E_{\text{ext}} = -2\pi V_{\text{cell}} \sum_{\mathbf{G} \neq \mathbf{0}} \sum_m Z_m \exp(-i\mathbf{G} \cdot \mathbf{R}_m) \frac{\hat{\rho}(\mathbf{G})}{|\mathbf{G}|^2} \quad (2.51)$$

The exchange-correlation potential, however, is typically determined in real space from the real space electron density $\rho(\mathbf{r})$. The Fourier coefficients $v_{\text{xc}}(\mathbf{G})$ are then obtained by Fourier transformation.

2.3.2 The projector augmented-wave method

One important obstacle in performing efficient electronic structure calculations is formed by the lowest energy electrons which are located close to the atomic nucleus (the core electrons). Due to their strongly localised nature, they need to be represented with much

finer resolution than the more extended valence electrons. Furthermore, the valence electron wave functions will show high frequency oscillations in the core regions,³ which are also numerically expensive to describe, especially in a plane wave basis set.

Many different approaches have been formulated in order to solve this problem. One attractive approach is the projector augmented-wave (PAW) method developed by Blöchl [52]. It uses the idea from augmented plane wave (APW) methods to divide real space into spherical regions centred around the nuclei and the remaining interstitial region. Inside these spheres, the wave functions are atomic-like and are efficiently described using atomic-like basis functions (e.g. the solutions of the Kohn-Sham equation for the isolated atom) on logarithmic radial grids. In the interstitial region, the wave functions vary more smoothly, so that a plane wave basis (or a uniform real space grid) is more advantageous. In the PAW method, the wave functions ψ_j are described as smooth wave functions ($\tilde{\psi}_j$) extending over the entire space to which corrections are added inside each “augmentation sphere” m :

$$|\psi_j\rangle = |\tilde{\psi}_j\rangle + \sum_{m=1}^M (|\psi_j^m\rangle - |\tilde{\psi}_j^m\rangle) \quad (2.52)$$

As mentioned already, a good choice for a “partial waves” basis ϕ_i^m for ψ_j^m is the solutions of the Kohn-Sham equation for the isolated atom. Their expansion coefficients happen to be the same as for their smooth counterparts $\tilde{\psi}_j^m$ expanded in a basis of smooth partial waves $\tilde{\phi}_i^m$ which match the partial waves outside the augmentation spheres. These smooth partial waves can be chosen to be polynomials [52, 46] or Bessel functions [53]. It is in this way possible to construct a complete and orthonormal set of smooth projector functions \tilde{p}_i^m that collect the expansion coefficients of the smooth part of the wave function inside the augmentation sphere:

$$|\tilde{\psi}_j^m\rangle = \sum_i \langle \tilde{p}_i^m | \tilde{\psi}_i \rangle |\tilde{\phi}_i^m\rangle \quad (2.53)$$

In this way the wave function can be written as:

$$|\psi_j\rangle = |\tilde{\psi}_j\rangle + \sum_{m=1}^M \left(\sum_i \langle \tilde{p}_i^m | \tilde{\psi}_i \rangle |\phi_i^m\rangle - \sum_i \langle \tilde{p}_i^m | \tilde{\psi}_i \rangle |\tilde{\phi}_i^m\rangle \right) \quad (2.54)$$

³This is a consequence from the requirement that the valence wave functions must be orthonormal to the core electron wave functions. This, in turn, is due to the wave functions being eigenfunctions of the Hamiltonian.

Similarly, the electron density can be seen as a smooth density plus atomic corrections:

$$\rho(\mathbf{r}) = \tilde{\rho}(\mathbf{r}) + \sum_{m=1}^M (\rho^m(\mathbf{r}) - \tilde{\rho}^m(\mathbf{r})) \quad (2.55)$$

Finding the electronic ground state is now reduced to variationally optimising the smooth part of the wave function only. For this quantity, the transformed Kohn-Sham Hamiltonian contains potential energy operators acting on the smooth density (evaluated using e.g. a plane wave basis set) plus corrections evaluated inside the augmentation spheres involving the partial waves and smooth partial waves (which can be evaluated efficiently using atom centered radial grids).

So far, the PAW method still provides an ‘all-electron’ description. In typical calculations, however, the frozen core approximation is invoked, which means the wave function for each frozen core state is considered constant and equal to its form of the reference atom. As sufficiently deep lying core states are typically quite inert in chemical processes, this is an efficient way of reducing the number of electrons that need to be explicitly taken into account. The atomization energies in the G2-1 data set, for example, have been shown to be affected by only a few meV/atom by this approximation [54]. Several additional approximations need to be made, such as truncating the (in principle infinite) number of (smooth) partial waves and projector functions, though also this can be done with very little loss in accuracy [52].

2.3.3 Finding the Kohn-Sham ground state

So far it has been assumed that the one-electron wave functions in the Kohn-Sham ground state are known. In general, this is not the case and an optimisation procedure is needed, starting from a certain initial guess. One can either look at this as a ‘variational’ problem of finding the wave function coefficients which minimise the total electronic energy, or as a ‘self-consistency’ problem of finding the coefficients for which the electronic energy is stationary.

In the latter scheme, it is often advantageous to take a superposition of atomic charge densities as an initial guess, from which the Kohn-Sham Hamiltonian is constructed for every \mathbf{k} -vector, from which the one-electron orbitals are obtained after diagonalisation. Using the occupied states a new charge density is then constructed. This is iterated until the energy has converged to within a certain threshold (typically 10^{-5} eV). This simple procedure is schematically represented in Figure 4.1 for the case of a plane wave basis set. As the procedure requires frequent transformations between real space and Fourier space,

it is crucial that the Fourier transformation is performed by an efficient algorithm.

This straightforward procedure, however, is inefficient, as direct diagonalisation of the large Hamiltonian matrix $H_{\mathbf{G},\mathbf{G}'}(\mathbf{k})$ is both computationally very costly and unnecessary. Typically one is only interested in the N lowest eigenstates, which is much less than the number of plane waves. Modern plane wave DFT codes therefore employ much more refined iteration schemes.

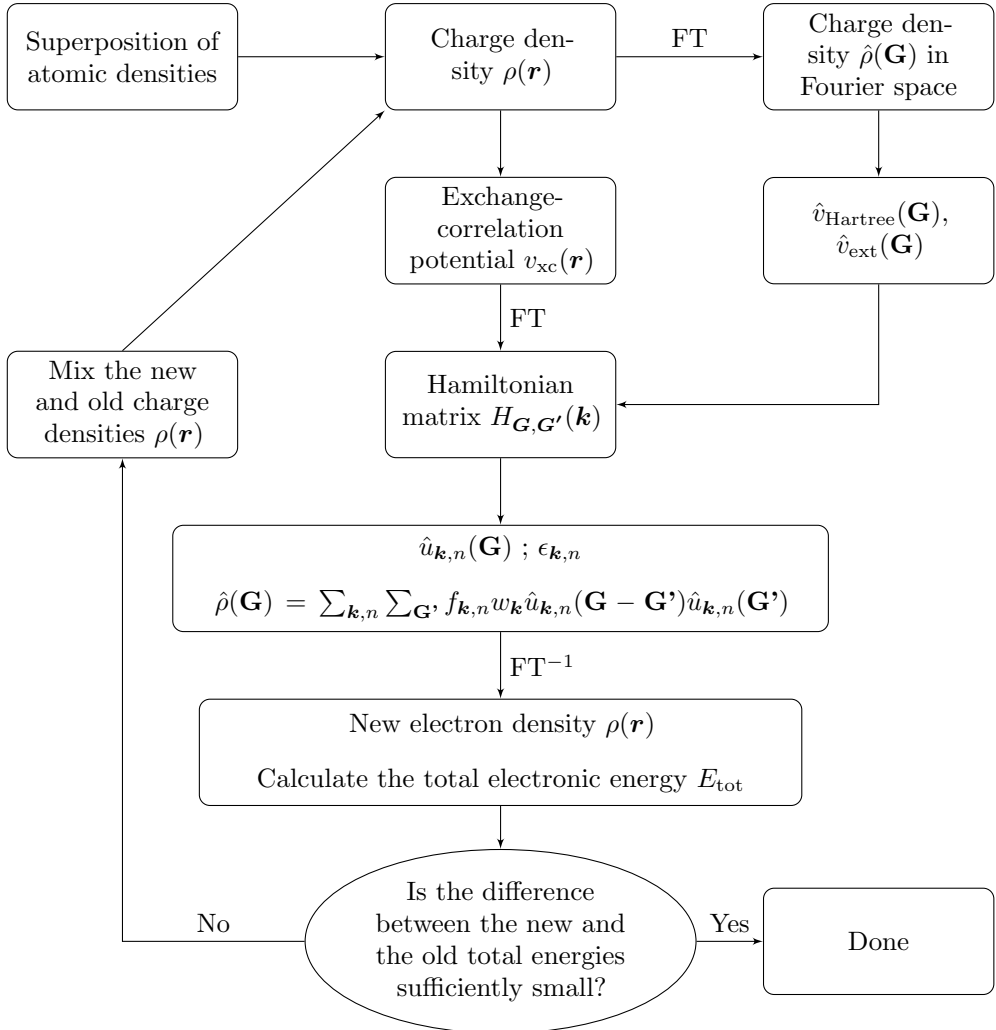


Figure 2.2: Flow chart showing how the iterative process of finding the Kohn-Sham ground state can be performed in a plane wave basis set.

Chapter 3

From electronic energies to measurable properties

This chapter deals with methods that make use of the first-principles description of the electronic structure to calculate various experimental observables, such as molecular structures, bond strengths, vibrational frequencies, reaction barriers and electronic binding energies.

3.1 Geometry optimisation

The most relevant molecular structures for many properties (such as the spectroscopic properties described in the coming paragraphs) are the ‘equilibrium geometries’ where the molecule adopts a (local) energy minimum with respect to displacement of the nuclei. Another type of configuration of particular interest in reaction rate theory are the ‘transition states’ corresponding to the minimum energy barrier separating reactants and products. Finding these two types of structures is routine and methods to do this are sketched in the next two sections.

3.1.1 Finding a local minimum

Finding the closest local minimum to a certain initial geometry guess is a matter of applying a suitable minimization algorithm to minimize the total energy with respect to the positions of the nuclei. Common algorithms are, for example, the conjugate gradient, damped molecular dynamics and quasi-Newton algorithms. All of these methods require determination of the forces f_i along each nuclear coordinate i :

$$f_i = -\frac{\partial E}{\partial R_i} \quad (3.1)$$

From the Hellman-Feynman theorem it can be shown that this force only depends on the charge density and the change in the Coulomb potential of the nuclei, i.e. just

classical electrostatic forces [55]:

$$f_i = - \int \rho(\mathbf{r}) \frac{\partial V_{\text{ext}}(\mathbf{r}, \mathbf{R})}{\partial R_i} d\mathbf{r} - \frac{\partial E_{i-i}}{\partial R_i} \quad (3.2)$$

The iterative process of computing the forces and generating successive structures is pursued until the norm of the force on each atom is below a certain limit. 10^{-2} eV/Å is for example a suitable, strict criterion. In my experience, the conjugate gradient algorithm tends to be the most efficient and robust option among the methods available in VASP, especially if the initial guess for the geometry is rather crude. If the structure is sufficiently close to a local minimum, the damped molecular dynamics method can be a faster choice.

3.1.2 Finding a transition state

The transition state for a reaction is defined as the lowest energy saddle point connecting the reactant(s) and the reaction product(s) (more on that in Section 3.3). Saddle points are local minima on the potential energy surface in all but the mode along which the reaction occurs, where the saddle point is a local maximum. In principle, the second derivatives of the potential energy would be helpful in finding such transition states, since the sign of a second derivative close to an extremum reveals whether that extremum in this direction is a maximum or a minimum. In plane wave DFT codes, however, these second derivatives are not readily computed (see Section 3.2), so different methods have been developed which rely only on first derivatives.

The nudged elastic band method

In the nudged elastic band (NEB) method [57, 58, 59], as the name suggests, the idea is to span an elastic band between the reactant state and the product state and to optimise this band so that it follows the minimum energy pathway between them. The procedure is started by constructing a band of intermediates and specifying the spring constant of the spring forces between successive intermediates in the band, so as to keep them equidistant. If the forces on the nuclei for each image are calculated, then following the components of the forces perpendicular to the band will lead to convergence towards the minimum energy pathway. A convenient variant is the climbing image NEB method, where, in addition, the energy of the highest intermediate is maximised and hence converges to the energy of the transition state.

The dimer method

The NEB method requires knowledge of the product state and involves ground state calculations for a large number of intermediates in order to resolve the minimum energy pathway. While it constitutes a rather robust method, it can be excessive if only information about the transition state is required. The dimer method [60] involves only two structures (the ‘dimer’), both slightly displaced from the center of the dimer along a particular direction. Through a series of translations and rotations of the dimer, the center of the dimer is moved to the nearest saddle point for the given initial direction. From the forces on the dimer structures, it is possible to estimate the rotation angle necessary to align the dimer along the direction with lowest curvature. One can translate the dimer following a modified force which points towards the saddle point.

My experience is that, although the dimer method tends to need more ‘force calls’ to converge to the saddle point than the NEB method, it can still result in a reduced computational cost thanks to the reduced number of structures. This is particularly the case when the minimum energy path is long and many intermediates are needed in the NEB method. One example where this problem may arise is the reaction of surface species with formation of a product in the gas phase. Another case where the dimer method can be useful is when the transition state and the imaginary mode are already known, but need to be re-evaluated using different computational settings (e.g., a larger unit cell, or a higher k-point density, or a different functional).

3.2 Vibrational frequencies

Molecules vibrate at characteristic frequencies, related to the molecular bond acting as a spring that counteracts a displacement of the atoms from their equilibrium positions. Estimating the vibrational frequencies can be useful for interpreting infra-red spectroscopy measurements and for evaluating the vibrational entropy and energy contributions to thermodynamic properties.

This is frequently done in the harmonic approximation. In this approximation, the displacements are assumed to be sufficiently small, so that the potential energy scales quadratically. The modes in which the atoms vibrate and their energy levels can then be obtained by diagonalising the mass-weighted Hessian matrix (see Appendix:A). Each mode has the following allowed energy levels:

$$E_{i,n} = \hbar\omega_i \left(\frac{1}{2} + n \right) \quad , \quad n = 0, 1, 2, \dots \quad (3.3)$$

If the molecule is isolated, six of these modes will have (near-)zero frequencies ω_i , corresponding to translation and rotation of the whole molecule (five in the case of a linear molecule). The remaining modes are associated with true vibrations, such as the stretching of the C-O bond in the CO molecule. In the case of modes with a negative energy curvature, as along the reaction coordinate at a saddle point, ω_i will be imaginary.

3.3 Rates of reactions on surfaces

Estimating the rates of elementary reactions from first principles is important to construct theoretical models that describe the preferred reaction mechanism for a chemical process. Also the catalytic activity of materials that are not yet experimentally synthesised can be evaluated in this way. One could, in principle, perform ab initio molecular dynamics simulations, explicitly propagating a collection of molecules on a surface, from which reaction rates can be extracted. This is, however, at present not an option, mainly because of the extremely wide separation of time scales between molecular vibrations ($\sim 10^{15}$ Hz) and activated chemical reactions (down to 1 Hz or less). This viewpoint, however, opens up possibilities for useful approximate theories [61, 62].

3.3.1 Transition state theory

A solution to the time scale problem is to *coarse-grain* the phase space that is sampled in the molecular dynamics simulations. There is little interest in the exact position and momentum every atom has, but rather whether a certain group of atoms on a particular adsorption site belongs to what is called adsorbate ‘X’. Defining the configuration α as the specification of each site i being occupied by an adsorbate j , then one can show, after assuming thermal equilibrium, that the probabilities $P_\alpha(t)$ of observing the specific configuration α at a certain time t obey a gain-loss type equation called the Master Equation:

$$\frac{\partial P_\alpha(t)}{\partial t} = \sum_{\beta} W_{\beta \rightarrow \alpha} P_\beta(t) - \sum_{\beta} W_{\alpha \rightarrow \beta} P_\alpha(t) \quad (3.4)$$

The ‘transition probability’ $W_{\alpha \rightarrow \beta}$ denotes the frequency in Hz at which a configuration α transforms into β . It can be shown that expressions for these transition probabilities are given by the ones familiar from conventional transition state theory (TST)¹ developed

¹For conventional TST the additional ‘no-recrossing’ approximation needs to be made [63], meaning that every trajectory crossing the phase space boundary between α and β actually results in the transformation to β . This is in general a very suitable approximation [64].

by Eyring [65], Evans and Polanyi [66]:

$$W_{\alpha \rightarrow \beta} = \frac{k_B T}{h} \frac{q_{\ddagger}}{q_{\alpha}} \quad (3.5)$$

$$W_{\beta \rightarrow \alpha} = \frac{k_B T}{h} \frac{q_{\ddagger}}{q_{\beta}} \quad (3.6)$$

The label \ddagger refers to the ‘transition state’, which corresponds to a saddle point on the energy landscape representing the minimum energy barrier the reactants (α) must overcome to form the products (β). The single-molecule partition functions q are typically evaluated² using simple statistical mechanical models (such as the quantum harmonic oscillator, rigid rotor, particle in a box) after assuming separability of e.g. translational, rotational, vibrational and electronic contributions to the total partition function (for further information, see e.g. Ref. [67]). The link to the well known Arrhenius equation [68] is easier to recognise if in Eq. (3.5) the electronic partition functions are evaluated with respect to their own potential energy minimum:

$$W_{\alpha \rightarrow \beta} = \frac{k_B T}{h} \frac{q'_{\ddagger}}{q'_{\alpha}} \exp\left(-\frac{E_{el,\ddagger} - E_{el,\alpha}}{k_B T}\right) \quad (3.7)$$

3.3.2 Mean-field kinetic modelling

The evolution of the adsorbate configurations on the surface, i.e. the probabilities $P_{\alpha}(t)$, can in principle be obtained by integrating the Master Equation (3.4), starting from a set of initial probabilities. As the number of possible configurations α is typically extremely large,³ direct numerical integration is infeasible. Kinetic Monte Carlo methods carry out the integration more efficiently through the use of stochastic techniques [69]. Since these methods come with a significant computational cost, usually simpler and more efficient (though potentially less accurate) procedures are employed based on the mean-field approximation. In this approximation, the adsorbates are assumed to be uniformly distributed over the whole surface, so that the probability of finding an adsorbate ‘A’ on a lattice site is the same and equal to its fractional coverage θ_A . This is only strictly justified if the surface is uniform, the diffusion of the adsorbates over the surface is sufficiently fast and lateral interactions (repulsive or attractive forces between adsorbates) are weak [70, 71]. This approximation allows to derive the typical rate equations from the Master Equation [61]. In the case of a bimolecular reaction between ‘A’ and ‘B’ adsorbates, the

²This is commonly done in a canonical ensemble so as to yield ‘Boltzmann’ transition frequencies, which have been averaged over the internal states of the reactants.

³For a surface with M sites and N adsorbates, the total number of configurations equals $(N + 1)^M$.

expression of the reaction rate is given by:

$$r = W\theta_{\text{AB-pairs}} \xrightarrow[\text{approximation}]{\text{mean-field}} r = WZ\theta_{\text{A}}\theta_{\text{B}} \quad (3.8)$$

Z is the coordination number of the lattice, i.e. the number of nearest-neighbour sites around a site. With a set of adsorbates and elementary reactions, the time evolution of the coverages $\boldsymbol{\theta}$ can be simulated together with the reaction rates \boldsymbol{r} by integrating the following set of coupled differential equations:

$$\frac{\partial\theta_i(t)}{\partial t} = \sum_j c_{ij}r_j(\boldsymbol{\theta}(t)) \quad (3.9)$$

with the coefficients c_{ij} the number of ‘ i ’ adsorbates consumed ($c_{ij} < 0$) or produced ($c_{ij} > 0$) in a reaction j . In this thesis the open-source SciPy Python package is used for to perform such numerical integrations, which wraps around the widely used odepack FORTRAN library [72].

3.4 Core-level spectroscopy

Core-level spectroscopy is a powerful technique to investigate the structure and chemical environment of the atoms close to the sample surface [73]. It uses X-ray photons to measure the binding energies of core electrons (e.g. the $3d_{5/2}$ level in Pd atoms), based on the photo-electric effect. Synchrotrons are often the preferred X-ray radiation sources, thanks to the high energy resolution and tunability of the X-ray beams [74].

Comparing the measured photo-emission spectrum with theoretical predictions for different structures has over the years proven to be a fruitful approach for elucidating surface structures and adsorbate geometries [75, 76, 77, 78]. Direct reproduction of the experimental binding energy spectrum is, however, rarely attempted, for two reasons. One is that absolute binding energies of core electrons with respect to e.g. the Fermi level are difficult to calculate with high accuracy. Secondly, also the precise line shape is difficult to reproduce, requiring e.g. time-dependent DFT or many-body perturbation techniques [79] such as the GW approach [80]. However, for interpreting core-level spectra without significant shake-up or shake-down satellites, it is sufficient to only calculate the relative shifts between the centers of the main peaks in the spectrum. These are referred to as the core-level shifts (CLS).

3.4.1 The complete screening picture

In the complete screening picture, the CLS is calculated as the energy difference:

$$\text{CLS} = [E_* - E_0] - [E_*^{\text{ref}} - E_0^{\text{ref}}] \quad (3.10)$$

with E_0 and E_* representing (valence) ground state energies of the unperturbed material and in presence of a core-hole in one of the atoms, respectively. This total energy approach relies on four main approximations regarding the final state, i.e. the electronic state of the material when the photo-electron has left the system:

- (1.) The core-hole has not yet decayed, i.e. its lifetime is long compared to the photo-emission process itself. This is indeed true in the case of not too heavy atoms and not too deep levels [81, 82, 83], where intra-atomic Auger decay of the core-hole is sufficiently slow [84].
- (2.) The valence electrons are considered to be in the ground state (with the constraint of a core-hole). Including this relaxation of the valence electrons is often crucial for accurately determining the CLS [85, 86, 87, 88].
- (3.) The remaining core electrons can be treated in different of ways: (i) by using pseudopotentials which have been generated for an ionised reference atom, (ii) by simply substituting the atom with the next element in the periodic table, the so-called ‘Z+1’ or ‘equivalent core’ approximation [89], and (iii) by removing the core state (in all-electron methods) and either relaxing the other core electrons (while maintaining orthogonality towards the core-hole) or keeping the remaining core electrons frozen (as done in the PAW implementation in VASP). These different methods yield similar results, although the ‘Z+1’ approximation only holds for sufficiently deep core-holes [90]. The reason for this similarity is that the relaxation of the core electrons is rather unimportant for the CLS, because this relaxation is quite independent of the chemical environment [91, 92].
- (4.) The effect of structural relaxation is neglected. Except for light atoms in molecules or light molecular adsorbates, these vibrational excitations in the final state do not contribute significantly to the apparent binding energy due to the slow response of the nuclei in comparison to the electrons [83].

As the use of periodic boundary conditions prohibits the use of charged supercells, charge neutrality needs to be maintained. This can be done either by adding an extra electron to the valence or by adding the compensating charge as a homogeneous ‘jellium’ background.

Adding an electron to the valence band is the better approach if there is a high density of states at the Fermi level, but is problematic for insulators and semiconductors, in which case the jellium background approach is preferred. In the jellium approach, the total electronic energy does not converge with respect to the vacuum distance between periodically repeated images. This would call for the application of dipole corrections [93, 94], but these corrections cancel out when the CLS is calculated between two atoms in the same unit cell. In that case the CLS expression reduces to:

$$\text{CLS} = E_* - E_*^{\text{ref}} \quad (3.11)$$

which has the additional benefit of accelerating the convergence with respect to k-point sampling, energy cutoff, inter-slab distance and slab dimensions [92].

3.4.2 Initial and final state contributions

In order to understand the origin of the CLS, it can be useful to decompose the CLS in so-called initial and final state shifts. The initial state contribution is related to differences in the charge density in the ‘initial’ ground state, whereas the final state contribution arises because of differences in the screening of the core-hole in the final state [73, 95]. While such a decomposition is to an extent arbitrary and only the total shift can be measured experimentally [96], it can be used to understand the origin of these shifts. Within Kohn-Sham DFT it is reasonable to associate the initial state shift with the negative of the shift in the core electron eigenvalue [97, 98]. The eigenvalue shift is furthermore closely related to the difference in electrostatic potential at the nuclei [99, 73, 95, 96].

Chapter 4

Reactions on surfaces

4.1 Catalytic reactions

The term ‘catalysis’ was coined in the early 19th century by the Swedish scientist Berzelius, for referring to phenomena where a small amount of a foreign substance has a great influence on the course of chemical reactions [100]. Early examples were Döbereiner’s experiments with ignition of a hydrogen-air stream using platinum powder [101]. The word derives from the ancient Greek verb καταλύειν meaning ‘breaking down’, implying that the catalyst decomposes the reactants and so facilitates the formation of the reaction products. Ostwald later offered a more precise definition of a catalyst: a substance that changes the rate of a chemical reaction without itself being consumed.

Catalysts can be classified as homogeneous, heterogeneous and enzymatic [102]. Homogeneous catalysts are part of the same fluid phase as the reactants, whereas heterogeneous catalysts (usually a solid surface) form a phase separate from that of the reactants. Enzymatic catalysts are a special case of homogeneous catalysis, referring to large, complex biomolecules. Of these three types, the heterogeneous catalysts possess the distinct advantage of being easy to separate from the reactant phase, which has led to innumerable industrial applications [103].

The first step in the heterogeneous catalytic process, as sketched in Figure 4.1, is the binding of the reactants from the fluid phase to the catalyst surface. Once they are adsorbed, molecules often undergo dissociation steps where they are separated into smaller fragments (e.g. O_2 dissociating into O atoms). After adsorption, the species can diffuse over the surface. When two reactants are in close proximity, reaction products can be formed. The catalytic cycle is completed by the desorption of these products into the fluid phase, with the surface sites becoming available again for reaction.

The reaction mechanism as depicted in Figure 4.1 is of the Langmuir-Hinshelwood type, where the products are formed by reactions between adsorbed species [104]. Another possibility is for gas phase species to directly react with adsorbates. This is the Eley-Rideal mechanism [105]. Yet another type, which frequently occurs on e.g. oxide catalysts, is the Mars-van Krevelen mechanism, where atoms of the substrate (e.g. lattice oxygen atoms)

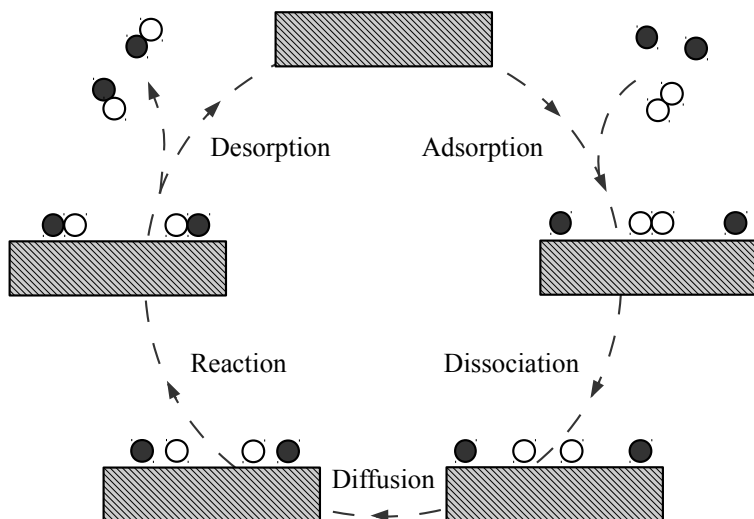


Figure 4.1: Diagram of a simple catalytic cycle for the reaction $A_2 + 2 B \rightarrow 2 AB$.

act as reactants and become part of product molecule [106].

The catalytic activity is known to be related to the adsorption strength of the adsorbates. This is, for example, stated in the Sabatier principle [107]. If the adsorbates are too strongly bound, they tend to be reluctant toward further reaction. If they are too weakly bound, their concentration on the surface is too low, which also reduces the reaction rate. For CO oxidation, for example, early transition metals and alkali (earth) metal oxides are usually not good catalysts, because the CO and/or O adsorbates are too strongly, resp. too lightly bound. Late transition metals and their oxides, however, typically display good activity [108].

4.2 Bonding on surfaces

In order to understand why adsorption strengths differ from one surface to the next, one needs to understand the main electronic interactions that are responsible for the bond formation. For this purpose, it is helpful to consider simplified molecular orbital ('MO') theories, such as the Hückel and extended Hückel methods [109]. Such approaches are basically Hartree-Fock theory using a minimal basis set (consisting of the MOs of the separate fragments) and with a number of approximations regarding the Fock matrix [110, 111].

In the following sections, the results of such an approach will be described for the example of CO binding to different surfaces. In order to illustrate different types of chemisorption bonds, three different substrates will be considered, namely Pd(100), PdO(101) and MgO(100). The following changes occur from palladium, over palladium oxide, to magnesium oxide:

- The bonding between the atoms in the surface evolves from metallic to ionic.
- The metal atoms become more and more depleted of charge.
- The band structure changes from metallic to semiconducting to insulating.

In order to capture the essence of the bonding only the two most relevant ‘frontier molecular orbitals’ for CO are examined, namely the 5σ and $2\pi^*$ MOs. These are the highest occupied and lowest unoccupied MOs (HOMO and LUMO), respectively. The 5σ MO can be regarded as a lone electron pair situated at the carbon end of the molecule, whereas the $2\pi^*$ MO has lobes on both the carbon and oxygen atoms (see Figure 4.2).

4.2.1 CO adsorbed on Pd(100)

Blyholder was among the first to apply MO analysis to bonding of CO to d -metal surfaces [114]. The most stable adsorption configuration for CO is the ‘bridge’ site between two Pd surface atoms, which is the one considered here. The ‘frontier MOs’ of the substrate are the valence bands of palladium, consisting of a wide sp -band and a more narrow d -band (see Figure 4.2). Both the 5σ and $2\pi^*$ MOs in CO interact strongly with the d -band, due to its higher density of states around the energy levels of the MOs.

The interaction of the 5σ MO with the d -band (mostly of d_{z^2} character, due to symmetry) gives bonding and anti-bonding combinations. As the anti-bonding combinations lie partly above the Fermi level, this has a net bonding effect. In this process the population of the 5σ MO is reduced – this is called ‘ 5σ donation’. There is also ‘ $2\pi^*$ backdonation’, as a result of the interaction between the $2\pi^*$ MO and the upper part of the metal d -band (mostly the d_{xz} and d_{yz}). Due to their higher energies with respect to the Fermi level, almost exclusively the bonding combinations get occupied, which contributes to the Pd-CO bond. The measured adsorption enthalpy of 1.7 eV [115] indeed shows that the CO binds strongly to the metal. As the population of the CO $2\pi^*$ MO increases and this MO is anti-bonding with respect to the C-O bond, this bond is weakened, leading to a larger C-O distance and a lower vibrational frequency [114].

This picture is captured in the d -band model of Hammer and Nørskov [116, 117], which is often used to explain variations between the adsorption properties of different d -metals.

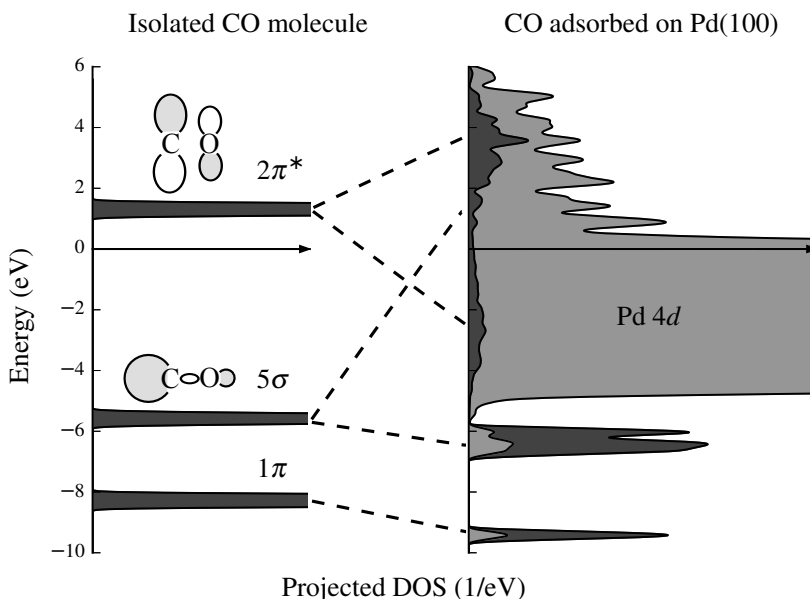


Figure 4.2: Density of states calculated with the PBE functional. Left: the density of states in the CO molecule. Right: the density of states projected on the CO s, p and Pd $4d$ states when CO is adsorbed in a bridge position on a Pd(100) surface slab.

The CO and O adsorption energies, for example, are dependent on the position of the d -band center: if the d -band is more than half filled, then moving the d -band center closer to the Fermi level will increase the interaction with unoccupied states of the molecule such as the CO $2\pi^*$ MO, which increases the adsorption energy. In this case, this increase is beneficial for the CO oxidation reaction. This explains why e.g. palladium is a better oxidation catalyst than gold, but also why steps and kinks are usually more reactive than the basal plane. Higher reactivity, however, does not necessarily imply higher catalytic activity, as explained by the Sabatier principle. Steps on palladium and platinum surfaces, for example, can be covered by strongly bound adsorbates, rendering them catalytically inactive [118].

4.2.2 CO adsorbed on PdO(101)

Owing to the transfer of charge from palladium to oxygen and the tetragonal crystal structure of PdO, the electronic structure of PdO differs in several ways from the metal.

The obvious differences are:

- A reduced d -electron count.
- A widening of the Pd d -band due to overlap with the O p states.
- The presence of a band gap, which is essentially formed by the Pd $4d$ states. The bulk band gap calculated with the HSE06 functional amounts to about 1 eV, and very similar values have also been measured experimentally [119, 120].

The calculated local valence density of states when CO is adsorbed atop of an undercoordinated Pd surface atom is shown in Figure 4.3. Due to the widening of the d -band and the atop position, there is better overlap with the CO 5σ MO, enhancing the bonding contribution of the σ donation. The backdonation from the metal d_{xz}, d_{yz} states, however, is hampered when the CO is adsorbed atop. Also in the bridge position, the backdonation can be expected to be reduced. This in part due to the band gap: as the d states with which the $2\pi^*$ MO interacts will have higher energies, less of the resulting bonding combinations will be occupied. The net result is that CO still binds rather strongly (an adsorption energy of 1.4 eV for the atop position, as calculated with the HSE06 functional), though less strongly than on the metal surface.

The above two effects can also be understood in a charge density picture. As the Pd atoms get oxidized, they become positively charged, which results in a higher affinity towards electron donation and a reduced tendency to donate electrons. These two phenomena have as consequences that (i) the bonding is not as strong as on the metal, and (ii) CO adsorbs preferably in atop rather than in bridge positions. Due to the slightly anti-bonding character of the 5σ MO with respect to the C-O bond [121], the C-O stretching frequency can actually increase compared to the gas phase [122].

4.2.3 CO adsorbed on MgO(100)

The charge separation is further enhanced when proceeding to MgO, which basically consists of Mg^{2+} and O^{2-} ions. The density of states at the MgO(100) surface is shown in Figure 4.4, which exemplifies the consequences of this charge transfer. The valence band is mostly made up of O $2p$ states, and the conduction band of unoccupied Mg $3s$ states.

When the CO molecule is situated above a Mg atom, donation can occur by interaction of the 5σ MO with the Mg sp states. The interaction, however, is weak and very little charge is transferred from the molecule to the surface. Backdonation to the $2\pi^*$ MO is practically non-existent. As a result, the adsorption strength is further reduced, to around 0.4 eV [123].

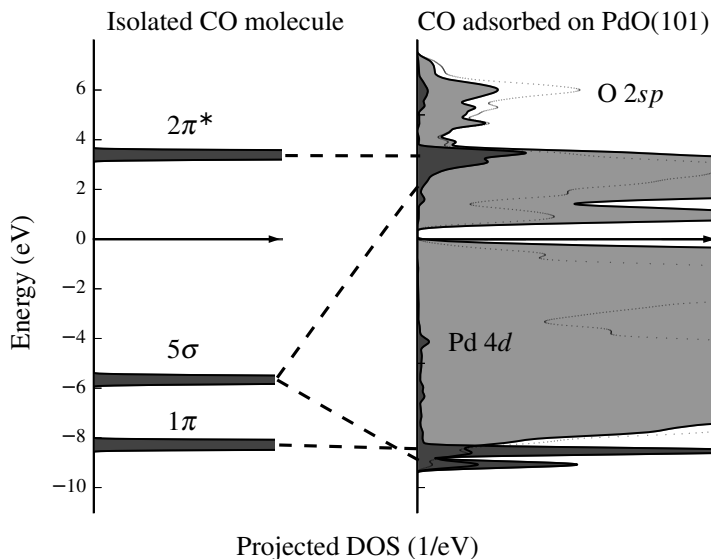


Figure 4.3: Density of states calculated with the HSE06 functional. Left: the density of states in the CO molecule. Right: the density of states projected on the CO s, p , Pd $4d$ and O s, p states when CO is adsorbed atop a threefold Pd atom in a PdO(101) slab.

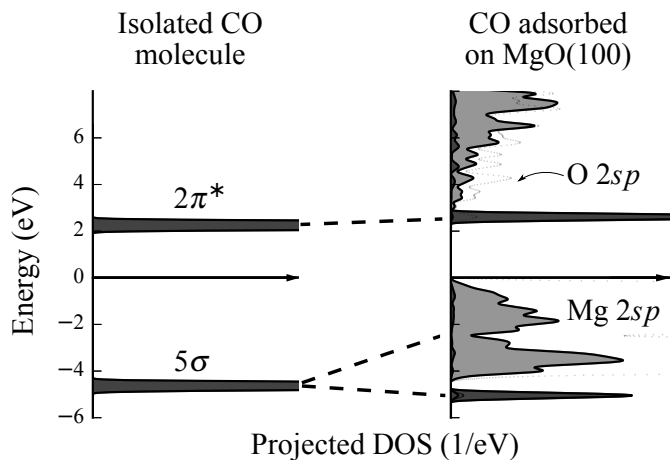


Figure 4.4: Density of states calculated with the PBE functional. Left: the density of states in the CO molecule. Right: the density of states projected on the CO, Mg and O s, p states when CO is adsorbed atop a Mg atom of a MgO(100) slab.

Chapter 5

Methane oxidation over PdO(101)

This chapter offers an introduction to methane oxidation over palladium and a summary of the appended papers. For an extensive overview of palladium-based catalysts for methane oxidation, the reader is referred to a review by Ciuparu and coworkers [6].

5.1 Introduction

The slow rate for the total oxidation of methane at low temperatures is mainly a kinetic problem. Thermodynamically, the process is favoured by a combustion enthalpy of over 9 eV per molecule [124], but the symmetry and strengths of the C-H bonds make the methane molecule difficult to activate. The issue of catalysing this process has a long scientific tradition, dating back to the early twentieth century [125]. Specific interest in the platinum group metals rose in the sixties [126, 127]. In particular, palladium-based catalysts were discovered to have high activities under oxidizing conditions, whereas platinum is better suited under reducing conditions.

Over the past decade, a consensus has grown that palladium is active both in a metallic and an oxidized form, and that the actual active phase depends on the reaction conditions [6, 128, 129, 130]. Palladium oxide seems to be the active form at moderate temperatures (below circa 950 K) and net oxidizing conditions. At higher temperatures and/or reducing conditions, the oxide is unstable and metallic palladium becomes the active material.

In the last years, further advances have been made regarding the activities of the different surface terminations of palladium oxide. DFT calculations indicate that the (100) orientation is the thermodynamically stable surface termination of the bulk oxide, followed by the (101) orientation [131] (see Figure 5.1 for structural models of these surface terminations). The difference in surface free energy between the two surfaces amounts to circa 30 meV/Å² at 600 K and an oxygen pressure of 1 atm [131]. There is also experimental evidence that the (100) orientation is the preferred surface orientation from bulk PdO [132, 133, 134, 135]. It is therefore surprising that the (101) orientation has been observed experimentally on e.g. Pd(100) [136, 129]. This can be explained by the small lattice mismatch between PdO(101) and the Pd(100) substrate, which makes

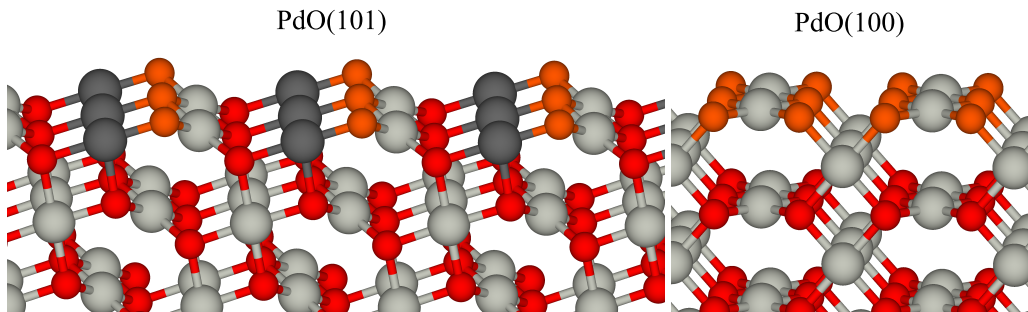


Figure 5.1: Ball-and-stick models of the PdO(101) and PdO(100) surfaces. The fourfold coordinated Pd and O atoms are coloured in respectively light gray and red. The threefold coordinated Pd and O atoms at the surface are given dark gray and orange colours.

it the most favourable orientation, at least for film thicknesses up to four PdO layers [137]. High-quality PdO(101) thin films can also be grown on Pd(111) by exposure to an atomic oxygen beam in ultrahigh vacuum, followed by annealing [138]. The formation of the oxide is preceded by a Pd_5O_4 ($\sqrt{6} \times \sqrt{6}$) surface oxide on Pd(111) [76, 139] (see Figure 5.2).

Owing to the stability of the methane molecule, the dissociative adsorption of methane is typically considered to be the rate-determining step in the methane oxidation process.¹ Theoretical investigations of the PdO(100) surface suggest that methane dissociation occurs with rather large energy barriers (1 eV or more) on this surface [140, 129]. The PdO(101) surface, on the other hand, displays much lower barriers for the initial dissociative adsorption (circa 0.5 eV with the PBE functional [129, 141, 142]). Importantly, the PdO(101) surface has been observed to be present during oxidation using in situ surface X-ray diffraction [129].

The topmost Pd atoms are coordinated differently on PdO(100) and PdO(101). On PdO(100) (Figure 5.1), the surface Pd atoms are coordinated to a rectangle of four neighbouring O atoms. In this configuration, the Pd d_{z^2} orbitals are less involved in the bonding with the O atoms compared to the other d -orbitals. This results in a high occupation of the d_{z^2} , which upon adsorption yields a repulsion towards the σ -type MOs on the methane molecule. The PdO(101) surface, however, contains threefold coordinated O and Pd atoms at the surface (Figure 5.1). Due to the different arrangement of O atoms around the threefold Pd atom, in particular the presence of an O atom directly below the Pd atom, there is now a significant depopulation of the d_{z^2} states. This reduces the repulsion towards the methane molecule.

¹At temperatures below 700 K, however, water desorption may become rate-limiting [6].

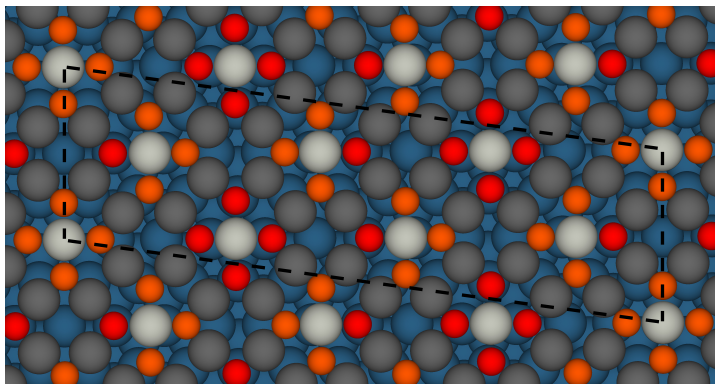


Figure 5.2: Structural model of the Pd_5O_4 ($\sqrt{6} \times \sqrt{6}$) surface oxide on Pd(111). The twofold and fourfold coordinated Pd atoms of the surface oxide are coloured in dark and light gray, respectively. The threefold and fourfold coordinated O atoms are coloured as orange and red.

Due to the significance of the PdO(101) surface, the interaction of various reagents with the surface has previously been investigated [143]. Temperature programmed desorption (TPD) experiments in combination with DFT calculations have for example shown that water strongly adsorbs on the undercoordinated Pd atoms and can dissociate with the formation of Pd-OH and O-H species [144]. Theoretical calculations indicate that also CO shows strong affinity for the surface Pd atoms CO [145, 136]. Species that are more weakly adsorbed on the undercoordinated Pd sites include O_2 [146], CO_2 [147] and small alkanes such as methane, ethane and propane [148, 141, 149, 150, 142, 151].

However, there is still an incomplete understanding of various aspects of the methane oxidation process over PdO(101). One question, for example, is the precise bonding configuration of intermediates to the surface, such as hydrogen and carbon monoxide. Moreover, the knowledge is limited concerning the subsequent pathways once methane is adsorbed and dissociated on the surface. Also the variation of the methane oxidation rate as a function of reaction conditions (i.e. the temperature and the gas-phase pressures of CH_4 , O_2 and H_2O) is not yet well understood in terms of elementary surface reactions. Lastly, there are also uncertainties on the theoretical side, such as the dependence of the computed properties of the PdO(101) surface on the choice of exchange-correlation functional. These are the types of questions addressed in this licentiate thesis.

5.2 Hydrogen adsorption

In **Paper I**, the interaction of the PdO(101) surface with molecular hydrogen is investigated. Experimentally, the prepared PdO(101) sample was cooled down to liquid nitrogen temperatures (circa 110 K) in high vacuum and subsequently exposed to 10 Langmuir H₂. Pd 3*d* and O 1*s* core-level spectra were measured before and after exposure. Computationally, various reactions of H₂ with the surface were explored, i.e. adsorption on threefold Pd sites, followed by dissociation and possible water formation. Comparing the measured and calculated Pd 3*d* and O 1*s* core-level shifts reveals that hydrogen indeed dissociates to form Pd-H and O-H species, as shown in Figure 5.3. The calculated energy barriers show that while H₂ dissociation is facile, relatively high energy barriers need to be overcome for the formation of water. This explains why water formation and reduction of the oxide surface is only observed at higher temperatures.

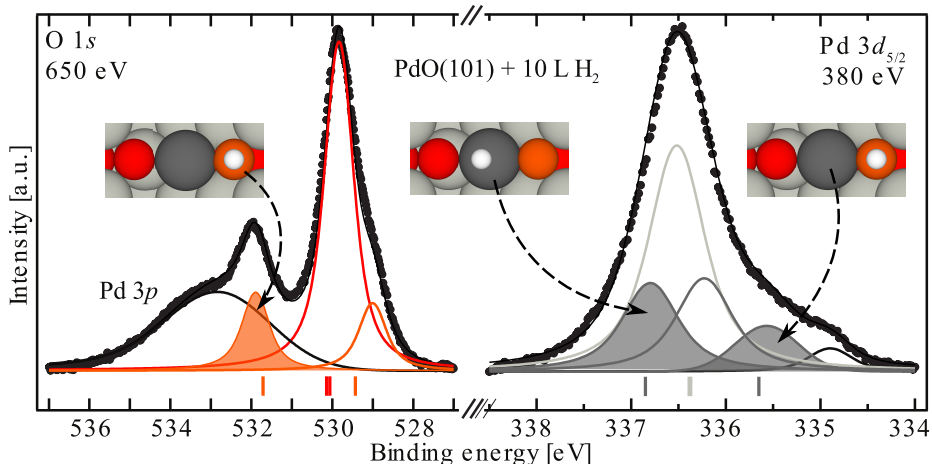


Figure 5.3: Measured core-level spectra from the O 1*s* (left) and Pd 3*d*_{5/2} regions. The calculated CLS with respect to bulk atoms are indicated by the lines underneath each spectrum. The new surface components that arise after H₂ exposure are shaded and are connected to the matching surface species.

5.3 Carbon monoxide adsorption

A similar approach is used in **Paper II** for the adsorption of CO. In addition, infrared spectroscopy data was measured and calculated in order to obtain complementary information. Theoretically, the most favourable adsorption sites for CO are the sites atop and bridge with respect to the threefold Pd atoms. Comparing the measured and

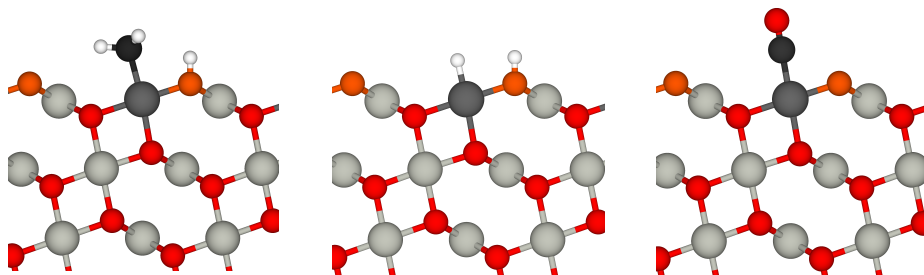


Figure 5.4: Ball-and-stick models of dissociatively adsorbed CH_4 and H_2 (left and center) and molecularly adsorbed CO (right) on the $\text{PdO}(101)$ surface. The PdO atom colours are as in Figure 5.1. The additional atoms C and H atoms are coloured in black and white, respectively.

computed core-level shifts and vibrational frequencies, it appears that both atop- and bridge-bound CO is present, with a majority of the former (see Figure 5.4).

Also CO adsorption on the $\text{Pd}(111)$ surface and the $(\sqrt{6} \times \sqrt{6}) \text{Pd}_5\text{O}_4$ surface oxide on $\text{Pd}(111)$ are considered in **Paper II**. An interesting aspect that is only briefly mentioned in the paper is the difference in the bonding of CO on the different surfaces. The CO adsorption energy in the atop sites on $\text{Pd}(111)$ and $\text{PdO}(101)$ are quite comparable (-1.38 eV and -1.49 eV, respectively, using the PBE functional). The charge difference plots shown in Figure 5.5, however, show that the origin for the strong binding to the oxide surface is different than on the metal. On the $\text{PdO}(101)$ surface, there is a significantly higher charge accumulation between the palladium and carbon atoms, indicating stronger 5σ donation as compared to the metal (cfr. Chapter 4). This compensates for the reduced backdonation to the $\text{CO } 2\pi^*$ MO. Adsorption on the surface oxide, however, is significantly weaker (-0.59 eV), which is also visible from the lower charge transfer. Here, the lack of underlying O atoms lead to insufficient depletion of $\text{Pd } s$ and d_{z^2} states, resulting in increased repulsion towards the CO molecule.

5.4 Methane oxidation

Paper III features a combination of experimental and theoretical work regarding the methane oxidation reaction over $\text{PdO}(101)$. Starting from a $\text{Pd}(100)$ single crystal surface, the temperature is raised from circa 440 K to 770 K in the presence of a 5:2 $\text{CH}_4:\text{O}_2$ gas mixture with a total pressure close to 1 mbar. Below 560 K, the $\text{O } 1s$ and $\text{Pd } 3d$ core-level spectra are characteristic of the $(\sqrt{5} \times \sqrt{5}) R27^\circ$ surface oxide over $\text{Pd}(100)$, which is equivalent to a single $\text{PdO}(101)$ monolayer on $\text{Pd}(100)$. The CO_2 partial pressure measured by mass spectrometry is very low, indicating that the surface oxide possesses

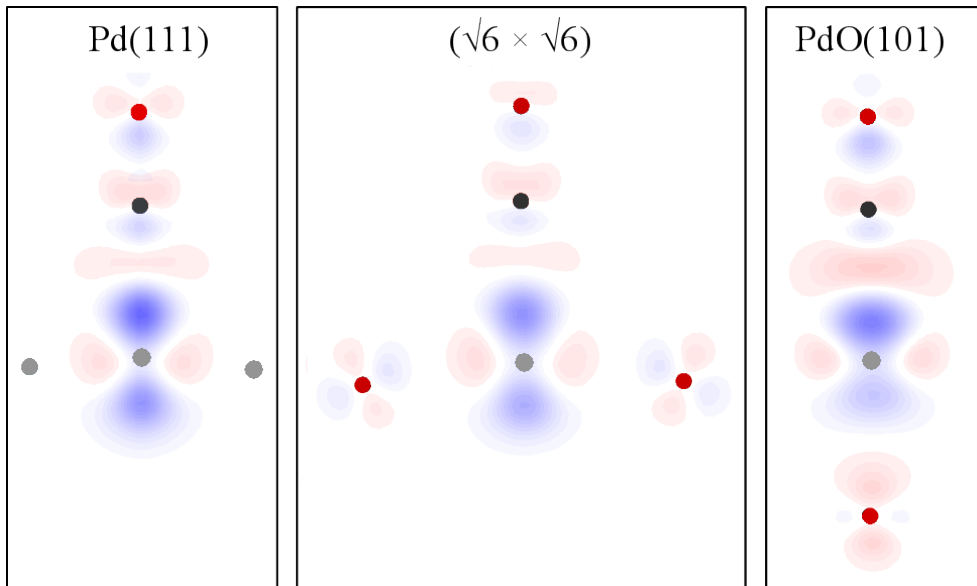


Figure 5.5: Charge density difference plots for CO adsorbed on atop sites of the Pd(111) surface, the $(\sqrt{6} \times \sqrt{6})$ surface oxide on Pd(111) and the PdO(101) surface. Red and blue regions represent charge accumulation and depletion, respectively.

low catalytic activity. When the temperature is raised further, the core-level signature of the PdO(101) surface emerges and catalytic activity increases.

The difference between the single-layer surface oxide and the multi-layer PdO(101) surface can again be related to the molecular structure. In the surface oxide, the oxygen atoms underneath the undercoordinated Pd atoms are absent, leading to an increase in the d_{z^2} states compared to the Pd atoms of the PdO(101) surface (see Figure 5.6). The resulting repulsive effect is visible in the higher electronic energy barrier for dissociation (1.34 eV versus 0.68 eV, using the PBE functional) and in the potential energy diagram for methane approaching the surface (see Figure 5.6).

In **Paper IV**, density functional theory and transition state theory are used to build a detailed kinetic model that describes the complete oxidation of methane over the PdO(101) surface. This model offers answers to several questions regarding the full reaction pathway of the methane oxidation process and its kinetic behaviour.

The high-temperature ($T > 700$ K) pathway for the conversion of methane can be described as follows. The methyl species produced by the dissociative adsorption of methane (see Figure 5.4) further react with the undercoordinated oxygen atoms, with CH_2 , CH_2O , CHO and CO as main intermediates. Oxygen is mainly incorporated into the molecule through reaction with oxygen atoms of the substrate, which supports a

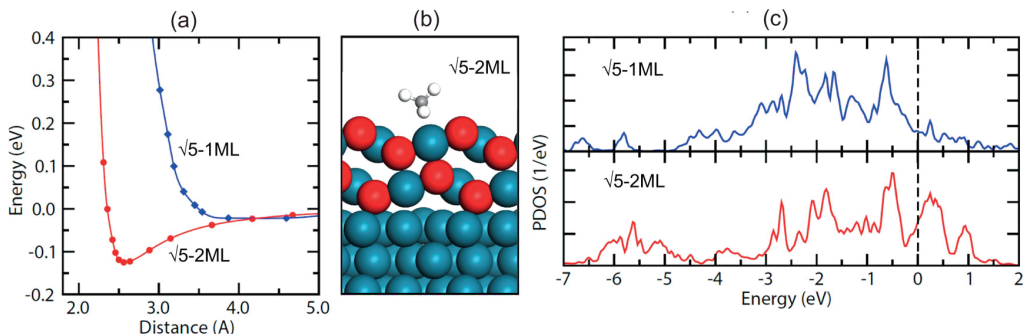


Figure 5.6: (a) Potential energy curves for CH₄ approaching the single and double ($\sqrt{5} \times \sqrt{5}$) oxide layers on Pd(100). (b) Structural model for CH₄ adsorbed on the two-layer PdO(101) surface oxide on Pd(100). (c) The density of states projected on the d_{z^2} states of the undercoordinated Pd atoms of the single and double ($\sqrt{5} \times \sqrt{5}$) oxide layers.

Mars - van Krevelen mechanism. The catalytic cycle is completed by reoxidation of the oxygen vacancies by O₂ adsorption and dissociation. Water production happens through reactions between surface hydroxyl groups. According to the model, the mechanism is slightly different at lower temperatures (600-700 K), where CH₃ preferably reacts with adsorbed O and further C-H dissociation steps mainly occur by reaction with adsorbed OH. Additionally, a second pathway for the dissociative adsorption of methane starts to contribute under these conditions, namely a route where methane reacts with the relatively abundant OH species, producing CH₃ and H₂O.

Interestingly, there appear to be strong attractive interactions between several species adsorbed on threefold Pd sites (such as CH₃, CH₂, CHO and OH) and H atoms adsorbed on threefold O sites. These interactions are on the order of 0.5 to 1 eV, which is very large compared to the thermal energy. This means that the mean-field approximation is not valid anymore. The adsorbates are no longer uniformly distributed over the surface, but their positions are correlated. The concentration of CH₃-H pairs during methane oxidation, for example, is several orders of magnitude higher than the concentration expected from the mean-field approximation. In **Paper IV** this is resolved through a quasi-chemical approach, where e.g. the CH₃ species are treated separately depending on whether or not they are paired with a H species.

Several interesting results are also obtained regarding the kinetic behaviour of the methane oxidation process. The dissociative adsorption of CH₄, for example, appears to be partly reversible under certain conditions. This is due to the relatively slow decomposition pathways for the adsorbed CH₃ species. The stability of these species is further enhanced

by the aforementioned attractive interaction between the CH_3 and H species. This phenomenon offers an explanation for the observed below-unity reaction orders in CH_4 pressure. As the methane pressure is raised, the concentration of H species increases, which traps a higher portion of the CH_3 species into $\text{CH}_3\text{-H}$ pairs. This, in turn, leads to a higher fraction of the methane molecules redesorbing before further oxidation can occur. Reaction orders of 0.6-0.7 have been measured experimentally [130], whereas values of 0.8-0.9 are predicted by the kinetic model.

This can also explain the variation in measured apparent activation energies in the mid to high temperature regimes. Above 750 K and at pressures in the Torr range, a low apparent activation energy of circa 0.3 eV has been observed [130]. In **Paper III**, at temperatures between 650 and 750 K and pressures in the mbar range, a value of circa 0.7 eV is measured. In both cases, the model predicts that the surface is essentially clean with a small amount of surface hydroxyl groups as the most abundant surface species, in agreement with the core-level measurements in **Paper III**. The apparent activation energies from the kinetic model are 0.27 and 0.78 eV, respectively, in agreement with the experiments.

At temperatures below circa 700 K and in the presence of water vapour, the surface is mostly covered by molecularly and dissociatively adsorbed H_2O , which inhibits the reaction rate. This is in agreement with the negative order in water pressure observed experimentally under those conditions [152] and leads to a further increase in the apparent activation energy to circa 1.3 eV. The value obtained from the kinetic model is 1.21 eV.

5.5 Computational methodology

Papers IV and V address certain questions regarding the computational methods used for describing the electronic structure of the $\text{PdO}(101)$ surface, in particular whether any properties are sensitive to the choice of the exchange-correlation functional. According to experiment, PdO is a semiconductor with a band gap of circa 1 eV [119, 120]. (Semi-)local functionals, however, such as LDA and PBE, describe PdO as a metal, albeit with a small density of states at the Fermi level [153, 154]. A Kohn-Sham band gap close to the experimental value does open up when including a fraction Hartree-Fock exchange in the exchange-correlation functional [137]. Although such hybrid functionals appear to offer a better description of PdO , it is not yet clear how sensitive calculated properties are to the detailed description of the electronic structure.

Paper IV addresses the functional dependence of reaction energies and energy barriers for a variety of reactions on the $\text{PdO}(101)$ surface by comparing results with the PBE

GGA and HSE06 hybrid functionals (at the PBE geometries). Compared to HSE06, the adsorption energy of several molecules is notably overestimated. The most severe difference occurs for the most stable O₂ adsorption configuration, which electronic adsorption energy is -1.25 eV in PBE but only -0.58 eV in HSE06. The significantly weaker adsorption with HSE06 is in much better agreement with O₂ TPD experiments performed on the PdO(101) surface [146, 143]. Weak O₂ chemisorption is also crucial in order to explain the near-zero reaction orders in oxygen pressure for the methane oxidation reaction. Also hydroxyl groups on the threefold Pd sites are much more stable in PBE (-3.01 eV in PBE versus -2.26 eV in HSE06, with respect to the gas phase). At the same time, due to the underestimation of the electron density on the surface oxygen atoms, the reactivity of the threefold oxygen atoms towards dissociation of e.g. CH₄, CH₃ and CH₂ is underestimated.²

Another difference that arises upon inclusion of Hartree-Fock exchange is the appearance of strong attractive interactions between several surface species. Many adsorbates adsorbed on the threefold coordinated Pd sites (such as OH, CH₃, CH₂ and CHO) are for example attracted towards H species on threefold O sites. These interactions are mostly negligible with the PBE functional, but are very strong if hybrid functionals are employed (on the order of 0.5 to 1 eV).

The shortcomings of GGA functionals such as PBE have also become apparent in the evaluation of certain core-level shifts for PdO(101). This is the topic of **Paper V**. For CO adsorbed atop on PdO(101), for example, the O 1s core-level shift between the adsorbed CO and the bulk oxide changes from circa +3 eV (PBE) to +4 eV (PBE0). While the latter is in good agreement with the value measured experimentally, the GGA core-level shift falls short of 1 eV. This finding contrasts with the experience regarding core-level shift calculations for clean and adsorbate-covered metal surfaces [86, 92, 91, 155] and surfaces of oxides such as SiO₂, GeO₂ and MgO [156, 157, 158]. The effect of the inclusion of the Fock exchange on the core-level shift can be connected to the sensitivity of the charge transfer towards electronegative atoms, such as O or F, on the exchange-correlation functional. In conclusion, when performing DFT calculations involving the PdO(101) surface, it is important to compare the results of standard (GGA) functionals with those of higher-level functionals such as hybrid functionals.

²The PBE+U approach with a Hubbard U correction of 5.5 eV to the Pd 4d states often yields results similar to the hybrid functionals, though the very high U value (compared to the band gap) makes this approach questionable.

Chapter 6

Conclusions and outlook

The main objective of this licentiate thesis is to reach a detailed understanding of the catalytic oxidation of methane over the PdO(101) surface. This is done by investigating the elementary surface reactions that occur when methane and other reactants interact with the surface. The used methodology is based on quantum-mechanical calculations using density functional theory (DFT), with different connections to experiments.

Several steps towards the objective have been achieved. By combining DFT calculations with spectroscopic measurements, it is shown that the PdO(101) surface provides sites for adsorption of H₂ and CO. H₂ dissociates easily to form H atoms bound to undercoordinated Pd and O atoms, whereas adsorbed CO is mainly found on top of the undercoordinated Pd atoms of the surface. Additionally, the important role of the oxygen atoms underneath the undercoordinated Pd atoms for methane oxidation was shown in a joint theoretical and experimental study. The ligand effect on the local electronic structure at the undercoordinated Pd surface atoms effectively explains the difference in activity between single- and multilayer PdO(101) thin films on Pd(100).

This work also contains an investigation of the full reaction mechanism by which methane is converted into carbon dioxide and water over the PdO(101) surface. A detailed kinetic model of this mechanism has been constructed that is able to describe many features of the methane oxidation kinetics in terms of elementary reactions on the PdO(101) surface.

Lastly, methodological contributions are made that highlight the sometimes limited accuracy of gradient-corrected density functionals in calculating reaction energies, energy barriers and core-level shifts involving the PdO(101) surface. Hybrid functionals are found to generally provide an improved description of these properties, though at a considerable additional computational cost.

In conclusion, the present work shows that it is possible to follow surface reactions and identify adsorbed species on palladium oxide surfaces by combining DFT calculations and carefully controlled experiments (most notably core-level spectroscopy). The combination of theory and experiment proved to have symbiotic effect. On one hand, the calculations have assisted in the interpretation of the experiments. On the other hand, the experimental

measurements have made it possible to evaluate the theoretical methodology. In this way, these combined studies have contributed to the understanding of the different types of binding sites on, in particular, the PdO(101) surface, as well as to progresses in the employed computational methodology. These two contributions, in turn, have allowed the subsequent construction of a detailed theoretical model for the oxidation of methane.

The results obtained so far have several implications. The detailed understanding of the different elementary surface reactions and their kinetic properties, for example, can provide inspiration for the design of new materials with improved catalytic activity. Also the advances in the understanding of the connection between the structure and the activity of the PdO(101) surface can be useful to this end.

Next, the methodological contributions have raised awareness about the importance of going beyond the generalised gradient approximation for a more accurate description of the properties of oxides that are erroneously described as metals within this approximation. Furthermore, the work shows that care needs to be taken in modelling surface kinetics on the PdO(101) surface, where the presence of strong adsorbate interactions leads to a breakdown of the mean-field approximation. This necessitates the use of methods that take into account the correlations between adsorbed particles. This information can also be of interest to experimental activity when kinetic parameters are deduced from reactor data.

6.1 Outlook

The results obtained in this thesis lead to several ideas for future research. Firstly, there are various other experiments that can be carried out on the PdO(101) surface. The possible intermediates of the methane conversion pathway, for example, have not yet received much attention. It might be possible to create methyl and methylene species on the surface by exposure to methyl halides and diazomethane, respectively. By combining these experiments with DFT calculations, these will have the aforementioned twofold benefit of broadening the knowledge of the PdO(101) surface chemistry and verifying theoretical predictions.

Another line of research will involve exploring modifications of the PdO(101) surface in order to improve its catalytic activity. For example, the local coordination of the undercoordinated Pd atoms of the (101) surface could be retained in a palladium oxide based mixed oxide. If in this way, e.g., the stability of water or methyl species on the surface can be reduced, the low temperature activity could possibly be enhanced. Another example would be to find oxide support materials that stabilise ultrathin PdO(101) films.

Also this approach could lead to a higher specific activity of PdO catalysts.

Finally, continuing the methodological aspect present in this work, it would be interesting to further explore the importance of e.g. lateral adsorbate interactions and surface diffusion limitations on different oxide surfaces.

Appendix

A Normal mode analysis

Obtaining the fundamental vibrational modes and their frequencies can be done as follows. Under the Born-Oppenheimer approximation, the nuclei move according to the time-dependent Schrödinger equation:

$$i\hbar \frac{\partial \Psi(t, \mathbf{R})}{\partial t} = H \Psi(t, \mathbf{R}) \quad (6.1)$$

where \mathbf{R} is a $3M$ -dimensional array that contains the three cartesian coordinates of each of the M nuclei. Since the Hamiltonian is not time-dependent, one can show by separation of variables that the time-dependent wave function is a superposition of the (phase-shifted) possible solutions $\Psi_j(\mathbf{R})$ of the time-independent Schrödinger equation:

$$\Psi(t, \mathbf{R}) = \sum_j c_j \Psi_j(\mathbf{R}) \exp(-iE_j t/\hbar) \quad , \quad \sum_j |c_j|^2 = 1 \quad (6.2)$$

$$H \Psi_j(\mathbf{R}) = \left(-\frac{1}{2} \sum_i \frac{1}{m_i} \frac{\partial^2}{\partial R_i^2} + V \right) \Psi_j(\mathbf{R}) = E_j \Psi_j(\mathbf{R}) \quad (6.3)$$

The kinetic energy term can be simplified by switching to the mass-weighted coordinates $r_i = m_i R_i$:

$$-\frac{1}{2} \sum_i \frac{1}{m_i} \frac{\partial^2}{\partial R_i^2} = -\frac{1}{2} \sum_i \frac{\partial^2}{\partial r_i^2} \quad (6.4)$$

The potential energy term can be simplified through a Taylor expansion around the equilibrium positions \mathbf{r}^0 :

$$\begin{aligned} V(\mathbf{r}) &= V(\mathbf{r}^0) + \sum_i \frac{\partial V(\mathbf{r}^0)}{\partial r_i} (r_i - r_i^0) \\ &\quad + \frac{1}{2!} \sum_{i,j} \frac{\partial^2 V(\mathbf{r}^0)}{\partial r_i \partial r_j} (r_i - r_i^0)(r_j - r_j^0) + \dots \end{aligned} \quad (6.5)$$

Since the structure is assumed to lie in a stationary point of the potential energy surface, the first derivative is zero. In the ‘harmonic approximation’ the Taylor expansion

is truncated to second order, which is justified if the displacements are sufficiently small. If furthermore the potential energy at the extremum is used as a reference, the expression for the potential becomes:

$$V(\mathbf{r}) \simeq \frac{1}{2} \sum_{i,j} \frac{\partial^2 V(\mathbf{r}^0)}{\partial r_i \partial r_j} (r_i - r_i^0)(r_j - r_j^0) \quad (6.6)$$

This can be written in matrix form, using the displacements $\mathbf{x} = \mathbf{r} - \mathbf{r}^0$:

$$V(\mathbf{r}) = \frac{1}{2} \mathbf{x}^T \mathcal{K} \mathbf{x} \quad (6.7)$$

The ‘Hessian’ matrix \mathcal{K} is the mass-weighted version of the Hessian in cartesian coordinates:

$$\mathcal{K}_{ij} = \frac{\partial^2 V(\mathbf{r})}{\partial r_i \partial r_j} = \frac{\partial^2 V(\mathbf{R})}{\partial R_i \partial R_j} / (m_i m_j)^{1/2} \quad (6.8)$$

The matrix elements are typically obtained using finite differentiation, i.e. by changing the i^{th} nuclear coordinate by a small amount Δ and calculating the forces on each nucleus with the electrons in their ground state:

$$\frac{\partial^2 V(\mathbf{R})}{\partial R_i \partial R_j} = \frac{\partial}{\partial R_i} \left(\frac{\partial V(\mathbf{R})}{\partial R_j} \right) = - \frac{\partial f_j(\mathbf{R})}{\partial R_i} \quad (6.9)$$

$$\simeq - (f_j(R_1, \dots, R_i + \Delta, \dots, R_{3M}) - f_j(R_1, \dots, R_i - \Delta, \dots, R_{3M})) / 2\Delta \quad (6.10)$$

The cross-terms ($i \neq j$) can be removed by diagonalising the (symmetric) Hessian using its matrix of eigenvectors \mathcal{P} and eigenvalues \mathcal{L} :

$$\mathcal{K} = \mathcal{P}^T \mathcal{L} \mathcal{P} \quad (6.11)$$

$$\Rightarrow V(\mathbf{R}) = \frac{1}{2} \mathbf{x}^T \left(\mathcal{P}^T \mathcal{L} \mathcal{P} \right) \mathbf{x} \quad (6.12)$$

$$= \frac{1}{2} (\mathcal{P} \mathbf{x})^T \mathcal{L} (\mathcal{P} \mathbf{x}) \quad (6.13)$$

This means that if an additional transformation to the new coordinates $\mathbf{y} = \mathcal{P} \mathbf{x}$ is performed, the potential energy operator takes on the simple form:

$$V(\mathbf{y}) = \frac{1}{2} \mathbf{y}^T \mathcal{L} \mathbf{y} = \sum_i \mathcal{L}_{ii} y_i^2 \quad (6.14)$$

After this orthogonal transformation, the expression for the kinetic energy operator

remains unchanged:

$$-\frac{1}{2} \sum_i \frac{\partial^2}{\partial r_i^2} = -\frac{1}{2} \sum_i \left(\sum_j \frac{\partial^2 y_j}{\partial r_i \partial r_j} \frac{\partial}{\partial y_j} + \sum_{k,l} \left(\frac{\partial y_k}{\partial r_i} \right) \left(\frac{\partial y_l}{\partial r_i} \right) \frac{\partial^2}{\partial y_k \partial y_l} \right) \quad (6.15)$$

$$= -\frac{1}{2} \sum_i \left(\sum_j 0 \frac{\partial}{\partial y_j} + \sum_{k,l} \mathcal{P}_{ki} \mathcal{P}_{li} \frac{\partial^2}{\partial y_k \partial y_l} \right) \quad (6.16)$$

$$= -\frac{1}{2} \sum_{k,l} \left(\sum_i \mathcal{P}_{ki} \mathcal{P}_{li} \right) \frac{\partial^2}{\partial y_k \partial y_l} \quad (6.17)$$

$$= -\frac{1}{2} \sum_{k,l} \delta_{kl} \frac{\partial^2}{\partial y_k \partial y_l} \quad (6.18)$$

$$= -\frac{1}{2} \sum_k \frac{\partial^2}{\partial y_k^2} \quad (6.19)$$

Equation (6.3) can now be rewritten as:

$$H \Psi_j(\mathbf{y}) = \sum_i \left(-\frac{1}{2} \frac{\partial^2}{\partial y_i^2} + \frac{1}{2} \mathcal{L}_{ii} y_i^2 \right) \Psi_j(\mathbf{y}) = E_j \Psi_j(\mathbf{y}) \quad (6.20)$$

It can easily be checked that the eigenstates $\Psi_j(\mathbf{R})$ of this Hamiltonian of a ‘ $3M$ -dimensional quantum harmonic oscillator’ can be written as a product of the eigenstates ψ_i of $3M$ independent one-dimensional oscillators:

$$\Psi_j(\mathbf{y}) = \prod_i \psi_i(y_i) \quad (6.21)$$

$$E_j = \sum_i E_i \quad (6.22)$$

$$H_i \psi_i(y_i) = \left(-\frac{1}{2} \frac{\partial^2}{\partial y_i^2} + \frac{1}{2} \mathcal{L}_{ii} y_i^2 \right) \psi_i(y_i) = E_i \psi_i(y_i) \quad (6.23)$$

These one-dimensional oscillators have as possible energy levels $E_{i,n_i} = \left(\frac{1}{2} + n_i \right) \omega_i$ with the quantum numbers $n_i = 0, 1, \dots$ and the frequencies $\omega_i = \sqrt{\mathcal{L}_{ii}}$.

Acknowledgements

The research presented in this thesis was carried out at the Division of Chemical Physics and the Competence Centre for Catalysis (KCK), Chalmers University of Technology, Gothenburg, Sweden, during the period of October 2012 to March 2015.

The Competence Centre for Catalysis is hosted by Chalmers University of Technology and financially supported by the Swedish Energy Agency and the member companies AB Volvo, ECAPS AB, Haldor Topsøe A/S, Scania CV AB, Volvo Car Corporation AB and Wärtsilä Finland Oy.

Funding by the Swedish Research Council (Vetenskapsrådet) in a Röntgen-Ångström project, by COST Action CM1104 and by Chalmers Areas of Advance Transport and Nanoscience and Nanotechnology, as well as CPU time granted by SNIC at C3SE (Göteborg) and PDC (Stockholm) are gratefully acknowledged.

Additionally I would like to express my gratitude to:

My main supervisor Henrik Grönbeck, for your guidance, supportiveness, for the many discussions (often both serious and humoristic at the same time) and for learning me both how to understand my results and how to communicate them.

My co-supervisor Anders Hellman, for luring me into this PhD project and for his own brand of humor.

My main collaborators from the experimental side – Natalia Martin and Edvin Lundgren. I have learned alot from your experiments and our discussions.

All (other) members of the Chemical Physics group, for creating a both pleasant and stimulating atmosphere. Special thanks go to several persons (in no particular order): Adriana, Jakub, Oliver, Simon, Igor, Pooya, Anna, Chris, and Adam.

All members of KCK, for showing the value of multidisciplinary, and special thanks to the director Magnus Skoglundh for his positive influence on the atmosphere in the centre.

Additional thanks for the good times go to Emma, Freddy, Mattias, Alexander, Sheedeh, Johan and Soran.

There are also people that are not easily put in one large category. Those are e.g. Déborah, Gülis, Ken, Viktor and FFF.

Last, but not least, I'm very grateful for the continuous support I receive from my family and for the ways they have helped me to shape my interests.

Bibliography

- [1] United Nations. *World Economic and Social Survey 2013: Sustainable Development Challenges*. 2013. URL: <http://www.un.org/en/development/desa/publications/world-economic-and-social-survey-2013-sustainable-development-challenges.html>.
- [2] European Commission. *Europe 2020 A strategy for smart, sustainable and inclusive growth*. 2010.
- [3] D. A. Lashof and D. R. Ahuja. *Nature* **344**, 6266 (1990), 529–531. DOI: 10.1038/344529a0.
- [4] D. T. Shindell et al. *Science* **326**, 5953 (2009), 716–718. DOI: 10.1126/science.1174760.
- [5] R. Kaufman and D. Stern. *Annual Estimates of Global Anthropogenic Methane Emissions: 1860-1994*. Tech. rep. 1998.
- [6] D. Ciuparu et al. *Catal. Rev.s* **44**, 4 (2002), 593–649. DOI: 10.1081/CR-120015482.
- [7] NGV Journal. *Worldwide NGV statistics*. URL: <http://www.ngvjournal.com/worldwide-ngv-statistics> (visited on 02/02/2015).
- [8] Göteborgenergi. *GoBiGas meets the growing need for biogas*. URL: <http://gobigas.goteborgenergi.se> (visited on 02/02/2015).
- [9] A. L. Polyzakis, C. Koroneos, and G. Xydis. *Energy Convers. Manage.* **49**, 4 (2008), 551–563. DOI: 10.1016/j.enconman.2007.08.002.
- [10] P. A. M. Dirac. *Proc. R. Soc. B* **123**, 792 (1929), 714–733.
- [11] P. Pyykko. *Chem. Rev.* **88**, 3 (1988), 563–594. DOI: 10.1021/cr00085a006.
- [12] R. M. Martin. *Electronic Structure: Basic Theory and Practical Methods*. Cambridge University Press, 2004.
- [13] L. H. Thomas. *Math. Proc. Cambridge* **23**, 05 (1927), 542–548. DOI: 10.1017/S0305004100011683.
- [14] E. Fermi. *Rend. Accad. Naz. Lincei* **6**, 6 (1927), 602–607.
- [15] P. Hohenberg and W. Kohn. *Phys. Rev.* **136**, 3B (1964), B864–B871. DOI: 10.1103/PhysRev.136.B864.
- [16] W. Kohn and L. J. Sham. *Phys. Rev.* **140**, 4A (1965), A1133–A1138. DOI: 10.1103/PhysRev.140.A1133.
- [17] G. B. Bacskay and S. Nordholm. *J. Phys. Chem. A* **117**, 33 (2013), 7946–7958. DOI: 10.1021/jp403284g.

- [18] T Koopmans. *Physica* **1**, 1-6 (1934), 104–113. DOI: 10.1016/S0031-8914(34)90011-2.
- [19] J. P. Perdew and M. Levy. *Phys. Rev. B* **56**, 24 (1997), 16021–16028. DOI: 10.1103/PhysRevB.56.16021.
- [20] J. P. Perdew and A. Zunger. *Phys. Rev. B* **23**, 10 (1981), 5048–5079. DOI: 10.1103/PhysRevB.23.5048.
- [21] D. M. Ceperley and B. J. Alder. *Phys. Rev. Lett.* **45**, 7 (1980), 566–569. DOI: 10.1103/PhysRevLett.45.566.
- [22] S. Kurth, J. P. Perdew, and P. Blaha. *Int. J. Quant. Chem.* **75**, 4-5 (1999), 889–909. DOI: 10.1002/(SICI)1097-461X(1999)75:4/5<889::AID-QUA54>3.0.CO;2-8.
- [23] R. O. Jones and O. Gunnarsson. *Rev. Mod. Phys.* **61**, 3 (1989), 689–746. DOI: 10.1103/RevModPhys.61.689.
- [24] L. A. Curtiss et al. *J. Chem. Phys.* **94**, 11 (1991), 7221–7230. DOI: 10.1063/1.460205.
- [25] L. A. Curtiss et al. *J. Chem. Phys.* **106**, 3 (1997), 1063–1079. DOI: 10.1063/1.473182.
- [26] M. Ernzerhof and G. E. Scuseria. *J. Chem. Phys.* **110**, 11 (1999), 5029–5036. DOI: 10.1063/1.478401.
- [27] J. P. Perdew et al. *Phys. Rev. B* **46**, 11 (1992), 6671–6687. DOI: 10.1103/PhysRevB.46.6671.
- [28] J. P. Perdew, K. Burke, and M. Ernzerhof. *Phys. Rev. Lett.* **77**, 18 (1996), 3865–3868. DOI: 10.1103/PhysRevLett.77.3865.
- [29] J. P. Perdew and M. Levy. *Phys. Rev. Lett.* **51**, 20 (1983), 1884–1887. DOI: 10.1103/PhysRevLett.51.1884.
- [30] D. Bohm and D. Pines. *Phys. Rev.* **92**, 3 (1953), 609–625. DOI: 10.1103/PhysRev.92.609.
- [31] X. Ren et al. *J. Mater. Sci* **47**, 21 (2012), 7447–7471. DOI: 10.1007/s10853-012-6570-4.
- [32] B. I. Lundqvist et al. *Int. J. Quantum Chem.* **56**, 4 (1995), 247–255. DOI: 10.1002/qua.560560410.
- [33] S. Lehtola and H. Jónsson. *J. Chem. Theory Comput.* **10**, 12 (2014), 5324–5337. DOI: 10.1021/ct500637x.
- [34] V. I. Anisimov, J. Zaanen, and O. K. Andersen. *Phys. Rev. B* **44**, 3 (1991), 943–954. DOI: 10.1103/PhysRevB.44.943.
- [35] M. Cococcioni and S. de Gironcoli. *Phys. Rev. B* **71**, 3 (2005), 035105. DOI: 10.1103/PhysRevB.71.035105.

- [36] I. Dabo et al. *Phys. Rev. B* **82**, 11 (2010), 115121. DOI: 10.1103/PhysRevB.82.115121.
- [37] J. P. Perdew, M. Ernzerhof, and K. Burke. *J. Chem. Phys.* **105**, 22 (1996), 9982–9985. DOI: 10.1063/1.472933.
- [38] C. Adamo and V. Barone. *J. Chem. Phys.* **110**, 13 (1999), 6158–6170. DOI: 10.1063/1.478522.
- [39] J. Paier et al. *J. Chem. Phys.* **124**, 15 (2006), 154709. DOI: 10.1063/1.2187006.
- [40] J. Paier et al. *J. Chem. Phys.* **125**, 24 (2006), 249901. DOI: 10.1063/1.2403866.
- [41] J. Jaramillo, G. E. Scuseria, and M. Ernzerhof. *J. Chem. Phys.* **118**, 3 (2003), 1068–1073. DOI: 10.1063/1.1528936.
- [42] J. Heyd, G. E. Scuseria, and M. Ernzerhof. *J. Chem. Phys.* **118**, 18 (2003), 8207–8215. DOI: 10.1063/1.1564060.
- [43] J. Heyd, G. E. Scuseria, and M. Ernzerhof. *J. Chem. Phys.* **124**, 21 (2006), 219906. DOI: 10.1063/1.2204597.
- [44] A. V. Krukau et al. *J. Chem. Phys.* **125**, 22 (2006), 224106. DOI: 10.1063/1.2404663.
- [45] J. J. Mortensen, L. B. Hansen, and K. W. Jacobsen. *Phys. Rev. B* **71**, 3 (2005), 035109. DOI: 10.1103/PhysRevB.71.035109.
- [46] J. Enkovaara et al. *J. Phys.: Condens. Matter* **22**, 25 (2010), 253202. DOI: 10.1088/0953-8984/22/25/253202.
- [47] F. Bloch. *de. Z. Physik* **52**, 7-8 (1929), 555–600. DOI: 10.1007/BF01339455.
- [48] H. J. Monkhorst and J. D. Pack. *Phys. Rev. B* **13**, 12 (1976), 5188–5192. DOI: 10.1103/PhysRevB.13.5188.
- [49] J. D. Pack and H. J. Monkhorst. *Phys. Rev. B* **16**, 4 (1977), 1748–1749. DOI: 10.1103/PhysRevB.16.1748.
- [50] M. Plancherel and M. Leffler. *it. Rend. Circ. Matem. Palermo* **30**, 1 (1910), 289–335. DOI: 10.1007/BF03014877.
- [51] C. Rostgaard. *arXiv:0910.1921 [cond-mat, physics:physics]* (2009).
- [52] P. E. Blöchl. *Phys. Rev. B* **50**, 24 (1994), 17953–17979. DOI: 10.1103/PhysRevB.50.17953.
- [53] G. Kresse and D. Joubert. *Phys. Rev. B* **59**, 3 (1999), 1758–1775. DOI: 10.1103/PhysRevB.59.1758.
- [54] M. Marsman and G. Kresse. *J. Chem. Phys.* **125**, 10 (2006), 104101. DOI: 10.1063/1.2338035.
- [55] R. P. Feynman. *Phys. Rev.* **56**, 4 (1939), 340–343. DOI: 10.1103/PhysRev.56.340.

- [56] D. Scholl and J. A. Steckel. *Density Functional Theory: A Practical Introduction*. Wiley VCH, 2009.
- [57] G Henkelman, B. Uberuaga, and H Jonsson. *J. Chem. Phys.* **113**, 22 (2000), 9901–9904. DOI: 10.1063/1.1329672.
- [58] G Henkelman and H Jonsson. *J. Chem. Phys.* **113**, 22 (2000), 9978–9985. DOI: 10.1063/1.1323224.
- [59] D. Sheppard, R. Terrell, and G. Henkelman. *J. Chem. Phys.* **128**, 13 (2008). DOI: 10.1063/1.2841941.
- [60] G. Henkelman and H. Jónsson. *J. Chem. Phys.* **111**, 15 (1999), 7010–7022. DOI: 10.1063/1.480097.
- [61] Jansen, A. P. J. *An Introduction to Kinetic Monte Carlo Simulations of Surface Reactions*. Vol. 856. Lecture Notes in Physics. 2012.
- [62] B. C. Garrett and D. G. Truhlar. “Chapter 5 - Variational transition state theory”. *Theory and Applications of Computational Chemistry*. Ed. by C. E. Dykstra et al. Amsterdam: Elsevier, 2005, pp. 67–87.
- [63] D. G. Truhlar and B. C. Garrett. *Acc. Chem. Res.* **13**, 12 (1980), 440–448. DOI: 10.1021/ar50156a002.
- [64] P. Pechukas. “Statistical Approximations in Collision Theory”. *Dynamics of Molecular Collisions: Part B*. Ed. by W. H. Miller. Vol. 2. Boston, MA: Springer US, 1976.
- [65] H. Eyring. *J. Chem. Phys.* **3**, 2 (1935), 107–115. DOI: 10.1063/1.1749604.
- [66] M. G. Evans and M. Polanyi. *Trans. Faraday Soc.* **31**, 0 (1935), 875–894. DOI: 10.1039/TF9353100875.
- [67] I. Chorkendorff and J. W. Niemantsverdriet. *Concepts of modern catalysis and kinetics*. John Wiley & Sons, 2006.
- [68] S. Arrhenius. *Z. Physik. Chem.* **4** (1889), 226.
- [69] D. T. Gillespie. *J. Comput. Phys.* **22**, 4 (1976), 403–434. DOI: 10.1016/0021-9991(76)90041-3.
- [70] V. P. Zhdanov. *Elementary Physicochemical Processes on Solid Surfaces*. Ed. by M. V. Twigg and M. S. Spencer. Fundamental and Applied Catalysis. Boston, MA: Springer US, 1991.
- [71] M. Van den Bossche. “Kinetic Monte Carlo modeling of the catalytic hydrogenation of benzene on Pt(111)”. Master thesis. Ghent University, 2012.
- [72] A. Hindmarsh. *IMACS Trans. Sci. Comput.* **1** (1983), 55–64.
- [73] K. Siegbahn and C. Nordling. *ESCA, atomic, molecular and solid state structure studied by means of electron spectroscopy*. 1967.

- [74] S. Mobilio, F. Boscherini, and C. Meneghini, eds. *Synchrotron Radiation - Basics, Methods and Applications*. Springer, 2015.
- [75] J. N. Andersen et al. *Phys. Rev. Lett.* **67**, 20 (1991), 2822–2825. DOI: 10.1103/PhysRevLett.67.2822.
- [76] E. Lundgren et al. *Phys. Rev. Lett.* **88**, 24 (2002), 246103. DOI: 10.1103/PhysRevLett.88.246103.
- [77] M. Todorova et al. *Surf. Sci.* **541**, 1-3 (2003), 101–112. DOI: 10.1016/S0039-6028(03)00873-2.
- [78] N. M. Martin et al. *J. Phys. Chem. C* **118**, 28 (2014), 15324–15331. DOI: 10.1021/jp504387p.
- [79] G. Onida, L. Reining, and A. Rubio. *Rev. Mod. Phys.* **74**, 2 (2002), 601–659. DOI: 10.1103/RevModPhys.74.601.
- [80] L. Hedin. *Phys. Rev.* **139**, 3A (1965), A796–A823. DOI: 10.1103/PhysRev.139.A796.
- [81] D. Nagel. “Interpretation of Valence Bond X-ray Spectra”. *Advances in X-ray Analysis*. Vol. 13. New York: Plenum Press, 1970, pp. 182–236.
- [82] F. C. Brown. “Ultraviolet Spectroscopy of Solids with the Use of Synchrotron Radiation”. *Solid State Physics*. Ed. by F. S. a. D. T. Henry Ehrenreich. Vol. Volume 29. Academic Press, 1974, pp. 1–73.
- [83] F. Bechstedt. *Phys. Status Solidi (B)* **112**, 1 (1982), 9–49. DOI: 10.1002/pssb.2221120102.
- [84] C. Noguera, D. Spanjaard, and J. Friedel. *J. Phys. F: Met. Phys.* **9**, 6 (1979), 1189. DOI: 10.1088/0305-4608/9/6/022.
- [85] E. Pehlke and M. Scheffler. *Phys. Rev. Lett.* **71**, 14 (1993), 2338–2341. DOI: 10.1103/PhysRevLett.71.2338.
- [86] J. N. Andersen et al. *Phys. Rev. B* **50**, 23 (1994), 17525–17533. DOI: 10.1103/PhysRevB.50.17525.
- [87] A. Pasquarello et al. “Core-Level Shifts in Si(001)-SiO₂ Systems: The Value of First-Principle Investigations”. *Fundamental Aspects of Ultrathin Dielectrics on Si-based Devices*. Ed. by E. Garfunkel, E. Gusev, and A. Vul. NATO Science Series 47. Springer Netherlands, 1998, pp. 89–102.
- [88] H. Grönbeck et al. *Phys. Rev. B* **85**, 11 (2012), 115445. DOI: 10.1103/PhysRevB.85.115445.
- [89] W. L. Jolly and D. N. Hendrickson. *J. Am. Chem. Soc.* **92**, 7 (1970), 1863–1871. DOI: 10.1021/ja00710a012.

- [90] W. F. Egelhoff Jr. *Surf. Sci. Rep.* **6**, 6-8 (1987), 253–415. DOI: 10.1016/0167-5729(87)90007-0.
- [91] L. Köhler and G. Kresse. *Phys. Rev. B* **70**, 16 (2004), 165405. DOI: 10.1103/PhysRevB.70.165405.
- [92] M. Birgersson et al. *Phys. Rev. B* **67**, 4 (2003), 045402. DOI: 10.1103/PhysRevB.67.045402.
- [93] G. Makov and M. C. Payne. *Phys. Rev. B* **51**, 7 (1995), 4014–4022. DOI: 10.1103/PhysRevB.51.4014.
- [94] J. Neugebauer and M. Scheffler. *Phys. Rev. B* **46**, 24 (1992), 16067–16080. DOI: 10.1103/PhysRevB.46.16067.
- [95] K. Siegbahn. *ESCA applied to free molecules*. North-Holland Pub. Co., 1970.
- [96] N. D. Lang and A. R. Williams. *Phys. Rev. B* **16**, 6 (1977), 2408–2419. DOI: 10.1103/PhysRevB.16.2408.
- [97] A. R. Williams and N. D. Lang. *Phys. Rev. Lett.* **40**, 14 (1978), 954–957. DOI: 10.1103/PhysRevLett.40.954.
- [98] D. Spanjaard et al. *Surf. Sci. Rep.* **5**, 1-2 (1985), 1–85. DOI: 10.1016/0167-5729(85)90003-2.
- [99] C. Nordling, S. Hagström, and K. Siegbahn. *Z. Physik* **178**, 5 (1964), 433–438. DOI: 10.1007/BF01379472.
- [100] J. Berzelius. *Jahres-Bericht* **4** (1823), 60–61.
- [101] P. Collins. *Platinum Metals Rev.* **30**, 3 (1986), 141–146.
- [102] S. T. Oyama and G. A. Somorjai. *J. Chem. Educ.* **65**, 9 (1988), 765. DOI: 10.1021/ed065p765.
- [103] G. Ertl et al., eds. *Handbook of Heterogeneous Catalysis*. 1st ed. John Wiley & Sons, Inc., 1997.
- [104] K. J. Laidler. *Pure Appl. Chem.* **68**, 1 (1996), 149–192. DOI: 10.1351/pac199668010149.
- [105] D. Eley and E. Rideal. *Nature* **146**, 3699 (1940), 401–402. DOI: 10.1038/146401d0.
- [106] P. Mars and D. W. van Krevelen. *Chem. Eng. Sci.* The Proceedings of the Conference on Oxidation Processes (1954), 41–59. DOI: 10.1016/S0009-2509(54)80005-4.
- [107] P. Sabatier. *Ber. Dtsch. Chem. Ges.* **44**, 3 (1911), 1984–2001. DOI: 10.1002/cber.19110440303.
- [108] H. Falsig et al. *Angew. Chem.* **120**, 26 (2008), 4913–4917. DOI: 10.1002/ange.200801479.
- [109] R. Hoffmann. *J. Chem. Phys.* **39**, 6 (1963), 1397–1412. DOI: 10.1063/1.1734456.

- [110] A. Leach. *Molecular Modelling: Principles and Applications*. 2nd ed. Pearson Education Limited, 2001.
- [111] T. A. Albright, J. K. Burdett, and M.-H. Whangbo. *Orbital Interactions in Chemistry*. 2nd ed. Wiley VCH, 2013.
- [112] R. Hoffmann. *Angew. Chem. Int. Ed. Engl.* **26**, 9 (1987), 846–878. DOI: 10.1002/anie.198708461.
- [113] R. Hoffmann. *Rev. Mod. Phys.* **60**, 3 (1988), 601–628. DOI: 10.1103/RevModPhys.60.601.
- [114] G. Blyholder. *J. Phys. Chem.* **68**, 10 (1964), 2772–2777. DOI: 10.1021/j100792a006.
- [115] R. J. Behm et al. *J. Chem. Phys.* **73**, 6 (1980), 2984–2995. DOI: 10.1063/1.440430.
- [116] B. Hammer and J. K. Nørskov. *Nature* **376**, 6537 (1995), 238–240. DOI: 10.1038/376238a0.
- [117] B. Hammer and J. K. Nørskov. “Theoretical surface science and catalysis—calculations and concepts”. *Advances in Catalysis*. Ed. by H. K. Bruce C. Gates. Vol. 45. Impact of Surface Science on Catalysis. Academic Press, 2000, pp. 71–129.
- [118] A. Trinchero, A. Hellman, and H. Grönbeck. *Surf. Sci.* **616** (2013), 206–213. DOI: 10.1016/j.susc.2013.06.014.
- [119] H. Okamoto and T. Asô. *Jpn. J. Appl. Phys.* **6**, 6 (1967), 779–779. DOI: 10.7567/JJAP.6.779.
- [120] P. O. Nilsson. *J. Phys. C: Solid State Phys.* **12**, 7 (1979), 1423. DOI: 10.1088/0022-3719/12/7/030.
- [121] H. H. Jaffé and M. Orchin. *Tetrahedron* **10**, 3-4 (1960), 212–214. DOI: 10.1016/S0040-4020(01)97808-1.
- [122] H. Jian-Wei et al. *Surf. Sci.* **261**, 1-3 (1992), 164–170. DOI: 10.1016/0039-6028(92)90228-X.
- [123] J.-W. He et al. *J. Vac. Sci. Technol. A* **10**, 4 (1992), 2248–2252. DOI: 10.1116/1.577926.
- [124] D. A. Pittam and G. Pilcher. *J. Chem. Soc., Faraday Trans. 1* **68**, 0 (1972), 2224–2229. DOI: 10.1039/F19726802224.
- [125] W. P. Yant and C. O. Hawk. *J. Am. Chem. Soc.* **49**, 6 (1927), 1454–1460. DOI: 10.1021/ja01405a010.
- [126] J. G. E. Cohn, J. A. J. Haley, and H. C. Andersen. “Method of effecting the catalytic contact of gases containing oxygen and methane”. Pat. US3056646 A. 1962.
- [127] R. B. Anderson et al. *Ind. Eng. Chem.* **53**, 10 (1961), 809–812. DOI: 10.1021/ie50622a024.

- [128] S. K. Matam et al. *J. Phys. Chem. C* **114**, 20 (2010), 9439–9443. DOI: 10.1021/jp1019697.
- [129] A. Hellman et al. *J. Phys. Chem. Lett.* **3**, 6 (2012), 678–682. DOI: 10.1021/jz300069s.
- [130] G. Zhu et al. *J. Phys. Chem. B* **109**, 6 (2005), 2331–2337. DOI: 10.1021/jp0488665.
- [131] J. Rogal, K. Reuter, and M. Scheffler. *Phys. Rev. B* **69**, 7 (2004), 075421. DOI: 10.1103/PhysRevB.69.075421.
- [132] J. R. McBride, K. C. Hass, and W. H. Weber. *Phys. Rev. B* **44**, 10 (1991), 5016–5028. DOI: 10.1103/PhysRevB.44.5016.
- [133] E. Lundgren et al. *Phys. Rev. Lett.* **92**, 4 (2004), 046101. DOI: 10.1103/PhysRevLett.92.046101.
- [134] A. Stierle et al. *J. Chem. Phys.* **122**, 4 (2005), 044706. DOI: 10.1063/1.1834491.
- [135] S. Penner et al. *J. Chem. Phys.* **125**, 9 (2006), 094703. DOI: 10.1063/1.2338028.
- [136] R. Westerström et al. *Phys. Rev. B* **83**, 11 (2011), 115440. DOI: 10.1103/PhysRevB.83.115440.
- [137] N. Seriani et al. *J. Chem. Phys.* **131**, 5 (2009), 054701. DOI: 10.1063/1.3187935.
- [138] H. H. Kan and J. F. Weaver. *Surf. Sci.* **602**, 9 (2008), L53–L57. DOI: 10.1016/j.susc.2008.03.007.
- [139] H. H. Kan and J. F. Weaver. *Surf. Sci.* **603**, 17 (2009), 2671–2682. DOI: 10.1016/j.susc.2009.06.023.
- [140] M. Blanco-Rey and S. J. Jenkins. *J. Chem. Phys.* **130**, 1 (2009), 014705. DOI: 10.1063/1.3046683.
- [141] J. F. Weaver et al. *J. Chem. Phys.* **132**, 2 (2010), 024709. DOI: 10.1063/1.3277672.
- [142] A. Antony, A. Asthagiri, and J. F. Weaver. *J. Chem. Phys.* **139**, 10 (2013), 104702. DOI: 10.1063/1.4819909.
- [143] J. F. Weaver. *Chem. Rev.* **113**, 6 (2013), 4164–4215. DOI: 10.1021/cr300323w.
- [144] H. H. Kan et al. *J. Phys. Chem. C* **113**, 4 (2009), 1495–1506. DOI: 10.1021/jp808008k.
- [145] J. T. Hirvi et al. *J. Chem. Phys.* **133**, 8 (2010), 084704. DOI: 10.1063/1.3464481.
- [146] J. Hinojosa Jose A., H. H. Kan, and J. F. Weaver. *J. Phys. Chem. C* **112**, 22 (2008), 8324–8331. DOI: 10.1021/jp800216x.
- [147] J. A. Hinojosa et al. *J. Phys. Chem. C* **116**, 4 (2012), 3007–3016. DOI: 10.1021/jp2104243.
- [148] J. F. Weaver, S. P. Devarajan, and C. Hakanoglu. *J. Phys. Chem. C* **113**, 22 (2009), 9773–9782. DOI: 10.1021/jp9013114.

- [149] J. F. Weaver et al. *Catal. Today* **160**, 1 (2011), 213–227. DOI: 10.1016/j.cattod.2010.06.012.
- [150] A. Antony et al. *J. Chem. Phys.* **136**, 5 (2012), 054702. DOI: 10.1063/1.3679167.
- [151] F. Zhang et al. *Surf. Sci.* **617** (2013), 249–255. DOI: 10.1016/j.susc.2013.07.022.
- [152] R. S Monteiro et al. *J. Catal.* **199**, 2 (2001), 291–301. DOI: 10.1006/jcat.2001.3176.
- [153] K. C. Hass and A. E. Carlsson. *Phys. Rev. B* **46**, 7 (1992), 4246–4249. DOI: 10.1103/PhysRevB.46.4246.
- [154] K.-T. Park et al. *Phys. Rev. B* **49**, 7 (1994), 4425–4431. DOI: 10.1103/PhysRevB.49.4425.
- [155] J. G. Wang et al. *Phys. Rev. Lett.* **95**, 25 (2005), 256102. DOI: 10.1103/PhysRevLett.95.256102.
- [156] A. Pasquarello, M. S. Hybertsen, and R. Car. *Phys. Rev. Lett.* **74**, 6 (1995), 1024–1027. DOI: 10.1103/PhysRevLett.74.1024.
- [157] J. F. Binder et al. *Phys. Rev. B* **85**, 24 (2012), 245305. DOI: 10.1103/PhysRevB.85.245305.
- [158] L. O. Paz-Borbón, A. Hellman, and H. Grönbeck. *J. Phys. Chem. C* **116**, 5 (2012), 3545–3551. DOI: 10.1021/jp209336q.

